THE EFFECT OF ATOMIC OXYGEN ON THE FORMATION OF INDIUM TIN OXIDE THIN FILMS

THESIS

Presented to the Graduate Council of
Texas State University-San Marcos
in Partial Fulfillment
of the Requirements

for the Degree

Master of SCIENCE

by

Nelson A. Simpson, B.S.

San Marcos, Texas
August 2013

THE EFFECT OF ATOMIC OXYGEN ON THE FORMATION OF INDIUM TIN OXIDE THIN FILMS

Committee Members Approved:

Wilhelmus Geerts, Chair

Edwin Piner

Ravi Droopad

Approved:

J. Michael Willoughby
Dean of the Graduate College

FAIR USE AND AUTHOR'S PERMISSION STATEMENT

Fair Use

Duplication Permission

For Mom and Dad -

I know you are both proud of me and thanks for all of your support

over these many years.

ACKNOWLEDGMENTS

I'd like to extend a very special thank you to all the professors and classmates that I have had the pleasure of being inspired by over the course of my academic career - I cannot thank all of you enough for being such an enormous source of support. Specifically, I would like to thank the following people:

Ms. Lauren Brown: *My lovely fiancé, for standing with me through all of the tough times and encouraging me to follow my dreams.*

Dr. Wilhemus J. Geerts: *For providing me such a great opportunity to learn and advance my knowledge.*

Eric Schires and Nathan England: *Who both patiently assisted me with all equipment related problems that I had and for providing such useful advice.*

This manuscript was submitted on May 17, 2013.

TABLE OF CONTENTS

Page

LIST OF FIGURES

Figure **Page**

LIST OF TABLES

Table **Page**

ABSTRACT

THE EFFECT OF ATOMIC OXYGEN ON THE FORMATION OF INDIUM TIN OXIDE THIN FILMS

by

Nelson Allen Simpson, B.S.

Texas State University-San Marcos

August 2013

SUPERVISING PROFESSOR: WILHELMUS GEERTS

Indium Tin Oxide (ITO) is a transparent conducting oxide that is used in flat panel displays and optoelectronics. Highly conductive and transparent ITO films are normally produced by heating the substrate to 300°C during deposition excluding plastics to be used as a substrate material. This thesis reports on an investigation whether or not dual ion beam sputtering can be used to create high quality ITO films at room temperature. The effect of exposing the sample to an atomic versus molecular oxygen flux during deposition was investigated. The vacuum chamber of the Texas State dual ion beam sputtering system was refurbished resulting in a lowering of the base pressure from $3x10^{-6}$ torr to $1.3x10^{-7}$ torr. Thin ITO films on glass and silicon substrates were made by reactive dual ion beam sputtering using an atomic oxygen assist beam and a molecular oxygen assist beam. The optical and electrical properties of the deposited films were characterized by ellipsometry and four point probe measurements. The film thickness and the ITO's optical

properties, i.e. refraction and extinction coefficient, were determined from the ellipsometry data for films sputtered at different oxygen flow rates (1-5 sccm). This data was used to calculate the resistivity and absorption coefficient of the sputtered ITO. The resistivity of the samples sputtered with atomic oxygen were lower than the resistivity for the samples made with molecular oxygen, achieving a minimum value of $2.67\text{x}10^{-3}$ Ωcm. This value is comparable to what has been obtained by others using ion beam sputtering. The figure of merit (FOM), i.e. σ/α, was calculated from the measurement data. The largest value obtained for the FOM was 0.08 Ω^{-1}. Films sputtered with atomic oxygen had a FOM which was systematically 1.2 to 5 times larger than films sputtered with molecular oxygen. Part of the work described in this thesis was presented at the spring 2012 meeting of the Texas Section of the American Physical Society.[1]

CHAPTER I: INTRODUCTION

Since first reported in 1907, transparent conducting oxides (TCO) have had a significant impact on modern industries such as Flat Panel Displays (FPD), solar cells, and heat-efficient windows.[2] A list of potential TCO materials include Al-doped ZnO, $GdInO_x$, SnO_2, and Sn-doped In_2O_3. The common characteristics of all of these materials, inherently high transparency (>85% over the visible spectrum) and useful electrical conductivity ($>10^3\ \Omega^{-1}cm^{-1}$), are achieved by selecting a wide-band gap oxide (E_g>3eV) that is rendered degenerate through the introduction of native and substitutional dopants.

Sn-doped In_2O_3, or Indium Tin Oxide, fits this layout very well with its ability to be doped by Sn substitutions and doubly charged oxygen vacancies. These vacancies form an impurity band that overlaps the conduction band, forming a degenerate semiconductor.[3] Indium Tin Oxide, or ITO, has a reported transmittance and conductivity as high as 95% and $1x10^4\ \Omega^{-1}cm^{-1}$ respectively, and was among the most widely used TCO's in 2012, with a market share of 93%.

To reach these transmittance and conductivity levels, ITO must be deposited at temperatures greater than $300°C$.[4] It is therefore difficult to deposit high quality ITO on inexpensive and light plastic substrates such as optical grade polymer, as these materials require a deposition temperature below 150°C.[3] At such low temperatures unactivated tin decreases the carrier density, resulting in a typical conductivity no better than $0.1\text{-}0.16x10^4\ \Omega^{-1}cm^{-1}$. High quality ITO films on plastic substrates could reduce the price per watt of solar cells and result in lighter and cheaper flat-panel displays and mobile devices that are less susceptible to

breaking.

The primary focus of this thesis is to investigate whether or not it is possible to deposit high quality ITO at room temperature by dual ion beam sputtering (DIBS), while exposing the sample to an atomic oxygen beam during deposition. Because the plasma used during DIBS is not directly in contact with the substrate and there is no need for the oxygen bonds to be broken, it is expected that deposition by DIBS might provide a means to deposit high quality ITO at low temperatures.

Although there is a substantial body of literature regarding the creation of ITO films, few studies investigate the efficacy of DIBS as a deposition method. Suzaki et al. used a DIBS system to investigate the effect of a helium assist beam on the growth of ITO thin films on Corning glass. Film resistivity was decreased by approximately a factor 2 by using a helium assist beam, although the data is very scattered.[5,6] A maximum conductivity of .14x10^4 Ω^{-1}cm^{-1} (n=5x10^{20} cm^{-1}, μ=16 cm^2/Vs) was also noted. In another study a mix of helium (100 sccm) and oxygen (1 sccm) was used in the assist beam. The resistivity and the transparency increased as a function of the assist ion beam voltage, the Hall mobility and the carrier concentration appeared to decrease. At higher assist beam voltages scanning electron microscope images indicated a rougher film surface, and X-ray analysis revealed a decrease in crystal grain size.[7] Lee et al.[8] investigated the effect of ion beam assisted sputtering by depositing samples by magnetron sputtering and exposing them to an argon ion beam during deposition. For low assist power (<40 W) an increase of the mobility and carrier density was noted and thus a strong decrease of the resistivity when increasing the assist power (.14x10^4 Ω^{-1}cm^{-1}). For assist powers above 40 W, the resistivity increased as the radiation damage strongly decreased the mobility more than it increased the carrier concentration.

Kim et al.[9] investigated the deposition of ITO films at low temperatures by argon ion beam sputtering using a single gun aimed at the target. The argon flow was kept at 4 sccm. Depositions were done for argon only and for a mix of argon and oxygen (Ar: 4 sccm; O_2: 0.5 sccm). Films were made as a function of the substrate temperature and as a function of ion beam energy. The highest conductivity films could be obtained with pure argon at 100°C (i.e. .66x10^4 $\Omega^{-1}cm^{-1}$).[10] Lucas et al. used ion beam sputtering to deposit ITO on Polyethylene Terephthalate (PET) at room temperature.[11] For room temperature depositions conductivities as high as 10^3 $\Omega^{-1}cm^{-1}$ were produced when an oxygen flux of 1 sccm of molecular oxygen was directed to the substrate. Another study utilized oxygen assist beams in combination with the evaporation of indium to create indium oxide thin films.[12] As these results refer to the undoped case it is difficult to compare the numbers; however, it was noted that there is an optimum oxygen flow and films deposited with lower beam energy have a higher conductivity.

To compare the quality of the films, one should not only look to the conductivity but also to the optical absorption of the films across the spectral range of interest. Thicker films in general have a lower sheet resistance but also a lower transmittance. The sheet resistance of a film, i.e. the ratio of the electric potential across the film and the current through the film per square area, depends on the conductivity σ of the material and the film thickness t. The conductivity σ of the material depends on carrier concentration n and the mobility μ:

$$R_s = \frac{1}{\sigma t} = \frac{1}{n\mu e t} \tag{1.1}$$

Since the conductivity is equal to the reciprocal value of the resistivity, ρ, the resistivity can be written as:

$$\rho = R_s t \tag{1.2}$$

The transmittance of a film, i.e. the ratio of the transmitted versus the incident intensity at a particular wavelength depends on the absorption coefficient of the material α and the thickness t of the film. The difference between the incident intensity and the sum of the reflected and transmitted intensity is the amount of light absorbed in the film. Beer-Lambert's law gives:

$$\begin{aligned} I_{absorbed} = I_{incident} - I_{reflected} - I_{transmitted} \Leftrightarrow \\ \frac{I_{absorbed}}{I_{incident}} = 1 - \left(\frac{I_{reflected}}{I_{incident}} + \frac{I_{transmitted}}{I_{incident}} \right) \Leftrightarrow \\ 1 - e^{-\alpha t} = 1 - (R + T) \Leftrightarrow \alpha t = -ln(R + T) \Leftrightarrow \\ \alpha = \frac{-ln(R + T)}{t} \end{aligned} \tag{1.3}$$

As electric dissipation is proportional to ρ and the optical absorption is proportional to α, then $\rho * \alpha$ is a measure for the total energy loss in the material, and it is clear from above equations that this ratio is independent of the film thickness and can be calculated from the reflection coefficient, the transmission coefficient, and the sheet resistance of the sample. Its reciprocal value is often used as a figure of merit for conductive transparent oxides:[2]

$$\frac{1}{\rho\alpha} = \frac{\sigma}{\alpha} = \left\{ R_s ln \left(\frac{1}{R + T} \right) \right\}^{-1} \tag{1.4}$$

Although σ/α is used in literature as a figure of merit for transparent conductive oxides, it does not take into account the reflection loss of the incident light. As R and T vary as a function of the wavelength, one normally takes the average value of R and T across the visible part of the spectrum. Table 1.1 summarizes the literature study above in terms of σ/α. It also lists the figure of merit of some other transparent conducting oxides.[2]

There is a substantial body of literature on the effect of the oxygen pressure

Table 1.1: **The Figure of Merit for some Common TCO's**

Material	Resistivity (Ωcm)	Visible Absorption(α)	Figure of Merit(Ω^{-1})
ZnO:In	-	0.20	0.2^2
SnO_2:Sb	-	0.12	0.4^2
In_2O_3:Sn	-	0.04	4^2
ZnO:Al	-	0.05	5^2
ZnO:F	-	.03	7^2
ITO: Magnetron Sputtering with Ar assist beam	7x10^{-4}, Room Temp[8]	-	-
ITO: Ion Beam Sputtering + Ar + O2	1.6x10^{-3}, Room Temp[9,10]	-	-
ITO: DIBS Ar in main beam + He in assist beam	7x10^{-4}, Room Temp[5]	-	-
ITO: IBS	1x10^{-3}, Room Temp, O_2 flow rate 1 sccm[10]	-	-
ITO: IBS	-	-	0.12[11]
ITO: PET	0.7X10^{-3}	-	4^{11}

on the properties of ITO films.[13,14] However, a search of the literature yielded no evidence of previous research on the effect of exposing the substrate during deposition to an atomic rather than molecular oxygen beam. To see if such changes can improve the electrical and optical properties of room temperature deposited ITO, two sets of samples were sputtered. One series was deposited while exposing the substrate to an atomic oxygen beam during deposition. The other series was deposited by exposing the substrate to a molecular oxygen beam during deposition. The quality of both types of samples was then determined from their measured optical and electrical properties using equation 1.4. Prior to the sample deposition for this research, it was discovered that the DIBS system had multiple leaks and sources of contamination. After it was repaired, the base pressure of the system was decreased by a factor of 12. This improvement allowed the production of reproducible ITO films.

The following chapters will provide information on vacuum systems and vacuum pumps, including the pumps that are used for dual ion beam sputtering in this project. They will also provide a list of modifications and repairs that were preformed on the system, including replacement of the sample holder drive chain. Informations will be provided about the DIBS process and the substrates that are used during this project. Following this, background will be provided on ellipsometry and the four-point probe technique. Finishing with the results of this project and our conclusions.

CHAPTER II: THE DIBS VACUUM SYSTEM

This section is to provide information about the conditions and methods that were used to create high vacuum in order to make the deposition of ITO possible in a controlled environment. In a vacuum system, atoms and molecules must be removed in order to achieve a lower pressure inside the system than that of the surrounding atmosphere. This high vacuum provides a better likelihood of allowing only the atoms and molecules of interest to be placed on the sample substrates. In order to achieve this vacuum, several different vacuum pumps were used. The following sections will describe the evacuation process and will discuss the different pumps used to achieve high vacuum.

Vacuum Basics

There are many different types of vacuum systems ranging from rough vacuum to high vacuum to ultrahigh vacuum. Table 2.1 shows the different degrees of vacuum and possible applications that require that degree of vacuum.

The type of sputtering used for this project was in the high vacuum range, to ensure that the space inside the chamber was as clean as possible and did not influence the chemical compositions of the sputtered films. The pressure ranges

Table 2.1: **Degrees of Vacuum and their Applications**

Rough Vacuum	**High Vacuum**	**Ultrahigh Vacuum**
Food Processing	Heat Treating	Space Research
Evaporation	Particle Acceleration	MBE
Sputtering	Vapor Deposition	Physics Research

most often associated with these levels of vacuum are listed in[15] table 2.2

Table 2.2: **Degrees of Vacuum and their Ranges**

Rough Vacuum	759 to 1x10$^-$3torr (approx.)
High Vacuum	1x10$^-$3 to 1x10$^-$8torr (approx.)
Ultrahigh Vacuum	Less than 1x10$^-$8torr

To reach the pressure needed multiple types of vacuum pumps were used to remove gas atoms and molecules from the main chamber. Before the air and other gases are pumped from the main chamber, the gas particles are moving at very high speed and colliding with each other. At atmospheric pressure the atoms in the chamber are densely packed together and the average distance a particle has to move before colliding with another particle is very short. This path length the gas molecules travel between two collisions is often referred to as the mean free path. Its value depends on the pressure and is given by equation 2.1.

$$Mean\ Free\ Path\ =\ \frac{5\text{x}10^{-3}\ torr\ cm}{P_{torr}} \tag{2.1}$$

Close to atmospheric pressure, collisions between particles happen much more frequently than collisions of the particles with the walls. Therefore, particle-particle interactions are the main factor that contributes to the motion of the particles within the chamber. In this state, the motion of the atoms and molecules is much like that of any fluid and is very predictable. This state is referred to as a viscous flow regime. Viscous flow conditions allow for the movement of great quantities of molecules per unit time from one place to another and also allows for the use of small diameter hoses and tubes for the evacuation of the chamber.

As particles are removed from the chamber the remaining molecules begin to interact less with each other and the mean free path increases with the decreasing pressure. If the mean free path of the gas molecules is less than the size of the

vacuum system the motion of the gas molecules becomes almost strictly random. This state is often referred to as the molecular flow regime. In the molecular flow regime, the particle movement is so unpredictable that the only way to increase the probability that one of these particles will reach the vacuum pump is to use larger hoses and larger inlets. Thus, the high vacuum pumps of the system, i.e. the turbomolecular pump and the cryopump, are connected by large valves to the main chamber, while the low vacuum roughing pumps are connected to the chamber by much smaller diameter tubes that have a length of several feet.

Roughing The Chamber

In order to efficiently evacuate the vacuum system, several different types of pumps were used. The first thing that needs to be done when evacuating the vacuum system is to "rough" the chamber. A mechanical pump, often referred to as a roughing pump, was used to "rough" the chamber and remove approximately 99.999% of the gas molecules from the vacuum chamber. A base pressure in the 10^{-3} torr range was obtained by roughing the chamber. Mechanical pumps work in the viscous flow regime by compressing the gas and venting it from the system. There are several types of roughing pumps, including oil-sealed roughing pumps and dry roughing pumps. Originally there were two mechanical pumps on the vacuum system: (1) a rotary vane oil-sealed mechanical pump used as a roughing pump for the chamber and the cryopump and (2) a Varian Tri-Scroll scrolling pump used to maintain the fore-line vacuum of the turbo pump. The oil-sealed mechanical pump was removed from the system and an additional valve was installed so the scroll pump could be used for roughing the chamber as well as maintaining the fore-line vacuum.

The typical scroll pump contains just a few components including but not

limited to a fixed scroll, an orbiting, scroll, a drive shaft and an electric motor (see Figure 2.1.) The design of the scroll pump is quite elegant. The motor turns the orbiting scroll around allowing for air to be trapped in between the fixed scroll and the orbiting scroll. The working process of this type of roughing pump is shown in Figure 2.2. The fixed and orbiting scrolls, which are identical, have axes of rotation that do not meet each other and are assembled at a relative angle of 180°. They contact each other at several touch lines and form a series of crescent-shaped chambers. The orbiting scroll rotates around its own axis in a planer motion. In Figure 3.2a the gas suction process is just finished; the center of the orbiting scroll is at 0°. At this position, the gas is trapped within the outer chamber. As the orbiting scroll rotates, the outer chamber becomes smaller and smaller, compressing the volume of gas. Figure 3.2b shows the center of the orbiting scroll being at 90°. At this position, the outer chamber is in the suction process, the middle chamber in the compression process, and the inner chamber in the discharging process. Figure 3.2c and d shows the suction and compression process in progress simultaneously.[16]

Scroll pumps are in general more expensive than oil-sealed pumps because scroll pumps require a relatively long lead-time regarding design, manufacturing and assembly. The accuracy of the two scrolls needs to be very high; therefore, the two scrolls are made at the same time and then matched by production number to ensure that the two parts are in tolerance of each other. Despite the added expense, the advantages are greater. Scroll pumps eliminate the possibility of oil back streaming into the system at low pressures. The ultimate pressures that can be achieved by scroll pumps are usually larger than that of oil-sealed pumps for this reason. The Varian Tri-Scroll pump that was used for this project allows for an ultimate pressure of 7×10^{-3} torr.[17] Scroll pumps also require minimum upkeep due to the fact that there are less moving parts. However, scroll pumps are not without disadvantages. Due to their design, which usually involves Teflon strips to make the

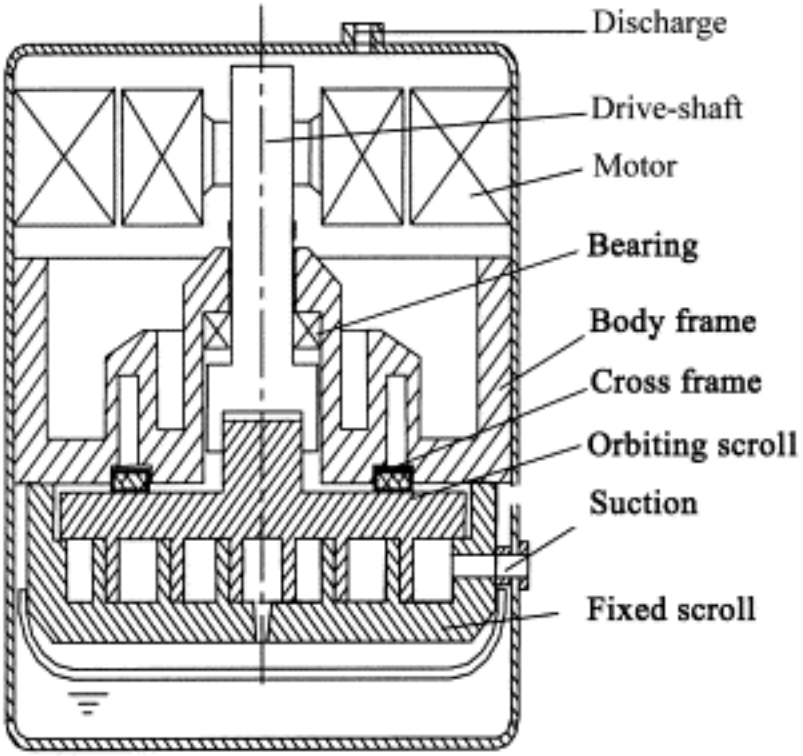

Figure 2.1: Typical Scroll Pump Diagram

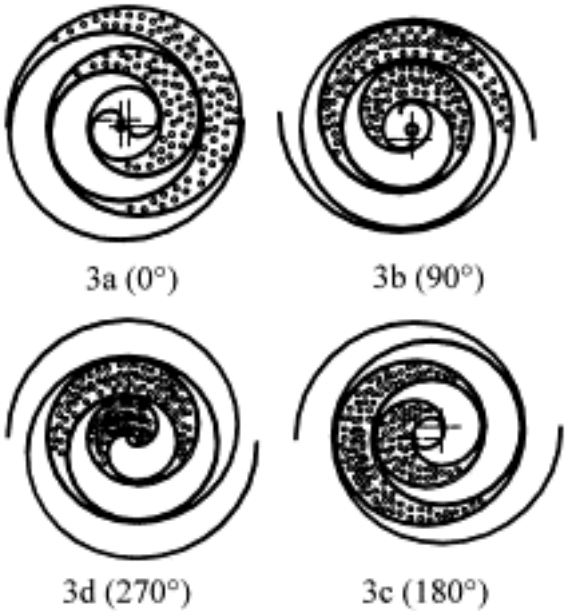

Figure 2.2: Pump Procedure of Scroll Pump

sill between the scrolls, scroll pumps are more vulnerable to any type of debris that is introduced into the scrolls. This may be seen as a loss of pumping speed.

Reaching High Vacuum

Having roughed the chamber, the flow of the molecules has changed from a viscous flow to a molecular flow. As mechanical pumps become very inefficient below 10^{-3} torr, other types of pumps needed to be used to further evacuate the system. At these low pressures the use of pumps that are operated with any type of oil is risky due to the chances of back streaming and possible contamination of the system. Therefore almost all of the high and ultra-high pumps do not contain any type of lubricant. The two high vacuum pumps connected to the system, the turbomolecular pump and cryopump, were oil free. Since the turbo pump cannot pump to atmospheric pressures, it requires a mechanical pump to be attached to its exhaust outlet. This pump takes the air exhausted by the turbo pump into the vacuum line between the two, called the fore-line, and compresses it further and then expels it from the system. Mechanical pumps are used for backing pumps because high vacuum pumps are designed to pump low pressures. High pressure on the backside of the pump can cause severe damage. The turbo pump attached to the DIBS system is backed by the Tri-Scroll Pump.

Turbomolecular pumps, are one of the few if not the only mechanical high vacuum pump that belongs to the category of kinetic vacuum pumps. Their design is similar to that of a turbine. A multi-stage, turbine-like rotor with bladed disks rotates in the housing. Interposed in the reverse direction between the rotor disks are bladed stator disks with similar geometries, as illustrated in Figure 2.3; the first blade is the rotor, the next is the stator, and so on. Each rotor and stator disk pair can be called a compression stage and a pump may have ten to forty stages. These

Figure 2.3: A Cut-Away of a Turbomolecular Pump

pairs collectively direct the molecules from the chamber into the pump and then out of the exhaust. The turbo pump is operated by a motor that has the capability to reach speeds of 90,000 rpm, depending on the size of the pump and the desired base pressure.

Because it is classified as a kinetic vacuum pump, a turbo pump reaches lower pressures by using momentum transfer. When a molecule strikes a moving surface, the moving surface imparts a portion of its momentum to the particle and changes its direction. In the molecular flow range, molecules will collide with the high speed blades of the pump more often than with each other. As a result of these collisions, each rotor blade imparts a portion of its momentum to the particles, speeding them up and changing their direction to flow into the next stage of the pump. This continues until the particles reach the mechanical pump.[15,18] The stages closer to the inlet of the pump have a larger angle to be able to pump faster, because more open space allows more access to the chamber. The stages closest to

the fore-line have a smaller angle for greater compression.

Though turbo pumps are extremely robust and reliable, they do have a few disadvantages that can cause the pump to completely fail. While they can be operated in pressures as high as 10^{-2} torr and could reach an ultimate pressure of $5x10^{-10}$ torr, operating at pressures higher than 10^{-2} torr can cause catastrophic failure. A turbo pump is designed to operate in the molecular flow range and if it is ever operated in the viscous flow range the force of all of the particles colliding with each other and the blades or the rotors can cause the blades to bend. This flexing, even if just slightly, can cause the rotors to slam into the stationary stators because of the small tolerances and distances between the two. With the rotors spinning so rapidly and the stators being stationary, this collision can cause the rotor blades to warp, even to the point of breaking. When this happens it is usually defined as a system crash. A crash can happen in one of two ways, the operation of the pump in high pressures or a system dump to atmosphere. Though most turbo pumps are robust enough to withstand a few of these situations, some newer pumps are able to automatically slow down or shut off if the pressures at either the inlet or the fore-line get too high. Another issue that arises with the uses of turbo pumps is the bearings that the rotors rotate on. During a system crash these bearings can become damaged and failure can occur at any time after the incident. If the pump is still in rotation when the system is used at high pressures or dumped to atmosphere, rotational lift of the blades can occur. As a result, the load on the bearings is lessened, which allows the bearings to come into contact with each other, permanently deforming, or "dimpling", them. Damaged bearings will force the pump to operate less smoothly and could eventually lead to vibration in the rotors. Proper venting of the turbo pump greatly reduces the risk of this happening.

The final pump on the DIBS system was the cryopump, which operates on a

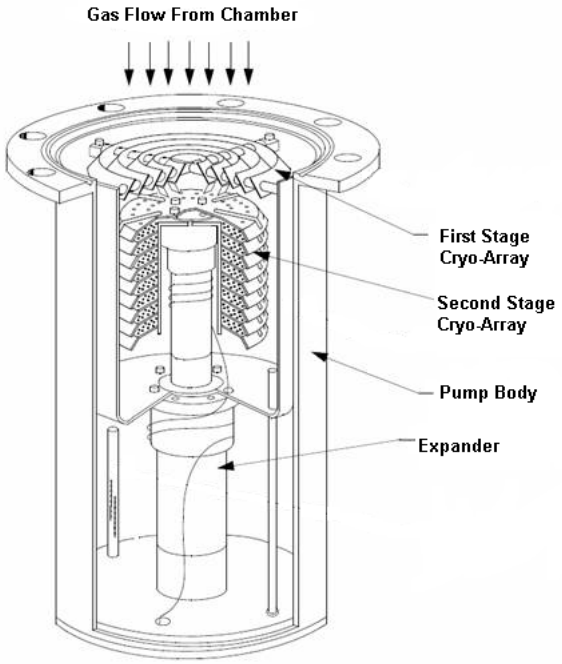

Figure 2.4: The Different Parts of a Cryopump

completely different principle than a mechanical pump. It contains a cryroarray that gets cooled down to between 13 and 16 K. At these temperatures gasses freeze out and become trapped in the pump. A cryopump is made up of two main components: the gas compressor and the pump module. The compressor and the cold head operate much like a refrigerator, but a cryopump is capable of much lower temperatures.

The pump module, as seen in Figure 2.4, consists of four major components: the expander, the first- and second-stage cryoarrays, and the pump body. All of the refrigeration occurs in the expander. High pressure helium gas, supplied by the gas compressor, is expanded in two stages to reach near cryogenic temperatures. The first stage typically operates between 50 and 80K. The second stage, or cryoarrays, operates between 10 and 20K.[15] The cryopump in the DIBS system contained cryoarrays operating at approximately 16.4K. Cryoarrays are the surfaces on which the gases are condensed or absorbed and consist of activated charcoal. The

expander provides the expanded helium gas that cools the arrays. Water vapor condenses by "cryocondensation" in the first-stage array. Other gases such as nitrogen, oxygen, and argon condense on the second-stage array, which operates at a temperature significantly below the boiling point of nitrogen gas. The arrays do no reach temperatures low enough to allow helium, hydrogen, and neon to condense on them. These gases are pumped by the use of cryosorption. Each layer of the second-stage array contains layers of activated charcoal which is very porous and acts as a maze-like structure for the gases in the chamber. As these gases start to get colder and flow through the charcoal they begin to lose thermal energy until they eventually stick to its surface. Finally, the pump body forms the vacuum-tight envelope which connects the pump to the vacuum chamber.

A cryopump is designed to be operated in a steady state mode to prevent gases and particles from returning into the chamber. As a result, cryopumps may eventually become saturated and lose pumping speed. The most common maintenance for cryopumps is the regeneration of the pump, which releases the trapped gases in the charcoal and pumps them out through the fore-line pump. A saturated cryopump can be diagnosed by closing the high vacuum valve and measuring the slope of the pressure versus time curve. If the slope is steeper than $1.66\text{x}10^{-4}$ torr/sec, the cryopump is dirty and should be regenerated. This is done by allowing the pump to heat up to room temperature in order to release the gases and then pumping them out using the rough pump. In the DIBS system this was done by switching off the compressor, flowing $1.29\text{x}10^{3}$ torr of N_2 gas and switching on the heater that was wrapped around the cryopump. During this process the temperature in the cryopump must be monitored and kept below 290-295 Kelvin or the indium gasket in the cryostat will become damaged. Once the temperature of the cryoarray reaches 290-295 K, the heater is switched off. For the DIBS system, regeneration only needs to happen once every year. After allowing the cryopump on

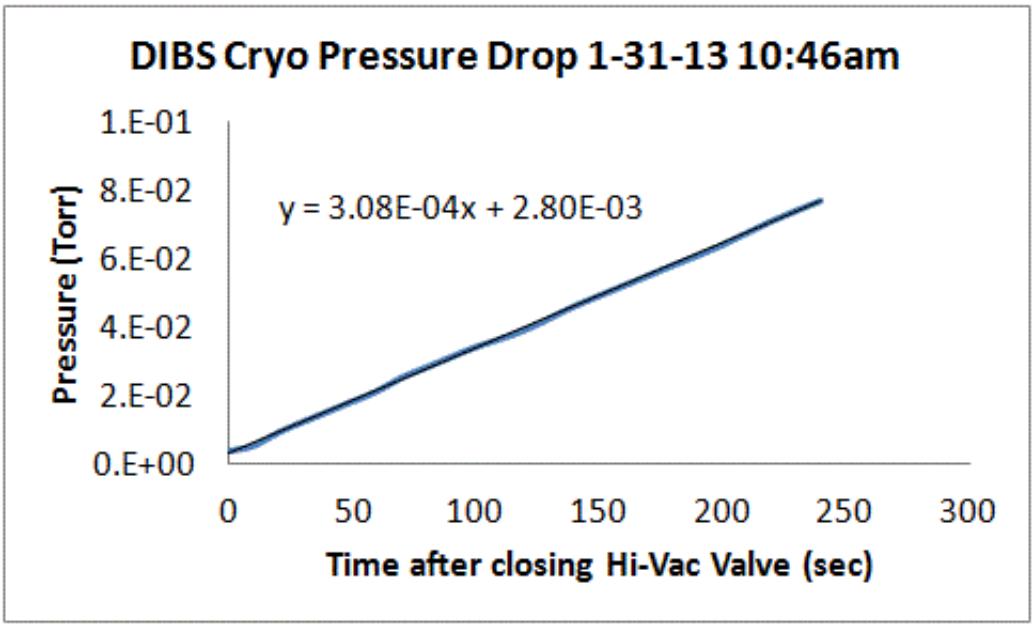

Figure 2.5: Rate of Rise Test for the Cryopump after Regeneration

the DIBS to regenerate, the rate of rise test was performed. Figure 2.5 shows a slope of $3.08\text{x}10^{-4}$ torr/sec, which is steeper than $1.66\text{x}10^{-4}$ torr/sec, indicating a saturated cryopump.

The Residual Gas Analyzer

Connected to the DIBS system is a residual gas analyzer (RGA) used to monitor the types of gases present in the chamber. A typical RGA has three major parts: an ionizer, a mass analyzer, and an ion detector. The output of an RGA is a spectrum that shows the relative intensities of the various species present in the gas. This output is known as a mass scan or mass spectrum. Figures 2.6 and 2.7 show outputs of the RGA used for this project and show a scan at the background pressure and a scan at the working pressure, respectively. Figure 2.6 demonstrates that the two dominate peaks in the background pressure were water at 19 AMU followed by nitrogen at 28 AMU. When the chamber was at working pressure, Figure 2.7 shows that argon had the two largest peaks at 40 and 20 AMU, along

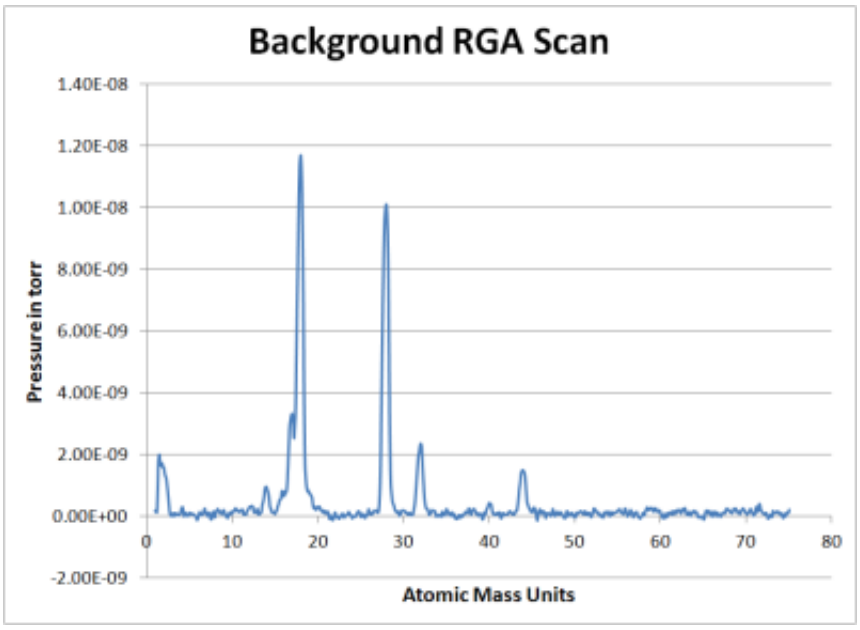

Figure 2.6: A RGA Scan at the Base Pressure of the System

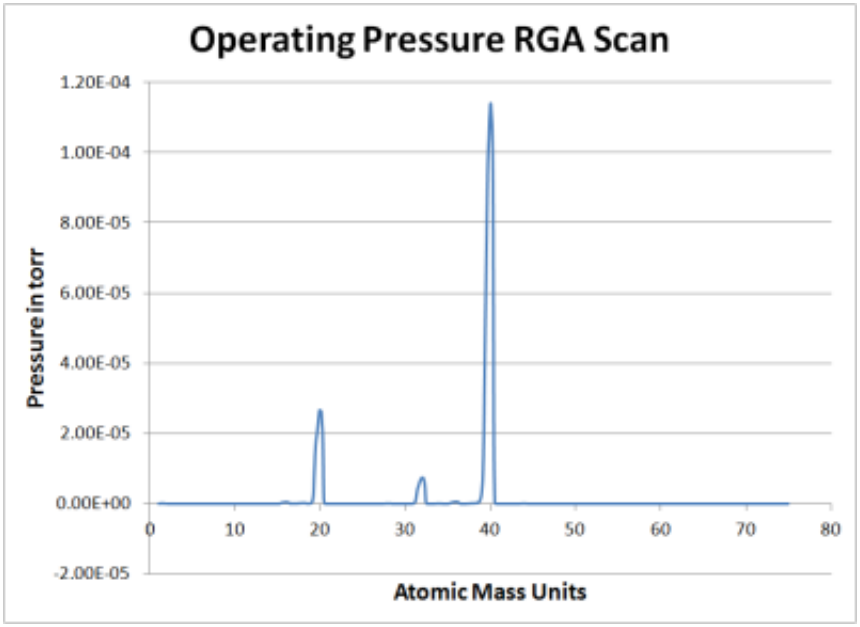

Figure 2.7: A RGA Scan at the Working Pressure of the System

with a small peak of oxygen at 32 AMU.

The ionizer, a hot emission filament, generates an ionizing electron beam which then ionizes the molecules of the gases in the chamber through electron impact ionization. The newly formed ions are counted by a radio frequency (RF) quadrupole in terms of their masses. The RF quadrupole has four cylindrical rods that are provided with combinations of AC and DC voltages of varying frequency. Only ions that possess the right mass-to-charge ratio can reach the ion collector for a given applied frequency. The mass scan of the RGA then plots the quantity of each molecule or atom present according to its unique mass-to-charge ratio. Within the design of the RGA this plot can be converted to the pressure of each molecule or atom versus the atomic weight of the element detected. The RGA for the DIBS system was mounted in between the turbo pump and the turbo high vacuum valve.[19]

The RGA can also be used to detect leaks in the vacuum system if it is configured to exclusively recognize the mass of helium atoms and molecules. By spraying helium gas over connections and flanges, the RGA will pick up any sudden increase in the presence of helium in the chamber, indicating a leak.

A disadvantage of the RGA is that the hot filament that ionized the gases can be destroyed when operated in the presence of reactive gases such as oxygen. For this experiment the RGA could not be operated during deposition of the samples to prevent any damages to the filament. It was operated momentarily, on occasion, to check the gas pressures of argon and oxygen immediately before deposition. Another disadvantage of the RGA is that the peaks exhibited by a mass spectrum must be interpreted properly. These readings can be ambiguous in certain cases, such as when two different molecules exhibit the same mass. Knowledge of how two different molecules with the same mass would dissociate into smaller fragments of different mass-to-charge ratios (known as cracking patterns) allows for

absolute identification of the gas.

Vacuum System Troubles

Once achieved, high vacuum systems are difficult to maintain due to leaks. They are filled with atoms and molecules moving around and colliding with each other. These free particles naturally strive to fill all the space available to them. Once a vacuum has been achieved, it becomes extremely difficult to keep these free particles out of the empty space. A vacuum system must be tightly sealed with rubber viton and copper seals in order to keep it isolated from the outside environment. The leading causes of vacuum troubles come from leaks in these seals or virtual leaks.

A vacuum cannot be achieved or maintained without proper sealing at connections and flanges. The proper seating of these seals are very important in preventing these types of leaks. Copper o-ring gaskets are used in parts of the system that need to be backed out or that get too hot during operation. The main ion gun in the DIBS system used these copper gaskets. Each time the gun was removed from the system, the gasket needed to be replaced. To seal a copper gasket the two flange pieces are bolted together and they each have a fine sharp edge that scores the copper gasket on either side. If the bolting process is not properly done, the gasket can become warped and will not seal correctly. Without a proper seal, the chamber may be pumped but the interior pressure will not be maintained once the pumps are turned off. Rubber gaskets help to ensure that the correct flange is sealed. Most connections that use these gaskets contain a groove in which the o-ring is placed. These gaskets must be changed regularly; if they dry out they do not maintain a proper seal. Also, these o-rings cannot be used at extremely low pressure due to out-gassing and they cannot be heated to high temperatures.[15]

Virtual leaks in vacuum systems can be common and also very difficult to locate. They stem from two sources, contaminants within the system or trapped air pockets. Virtual leaks caused by contaminants, often oil and dirt from fingerprints, are often referred to as out-gassing or desorption. These contaminants will expand tremendously within the vacuum increasing the pressure in the chamber. Virtual leaks can be prevented by only placing clean objects in the chamber and by touching the minimum amount of surfaces inside as possible. The second type of virtual leak, trapped air pockets, are quite possibly the hardest type of leak to find in a vacuum system. This leak happens when there is a trapped air pocket that has a very narrow path to escape into the vacuum. Any opening in the system that provides enough space for an atom or molecule to pass through can also trap residual gas molecules, ultimately increasing the pressure in the system. This type of leak is most often caused by any type of bolts that are used inside the system. When a bolt hole is drilled, the depth of the hole is longer than the bolt; as a result, when the bolt is placed into the hole and tightened there is a small air pocket that is trapped. The threads of the bolt allow a narrow space for this pocket to escape through, though not quickly. This type of leak can take an extremely long time to evacuate and is very difficult, time consuming, or even impossible to find. Vented bolts, which contain a vent hole the entire length of the bolt, allow for the trapped pocket to be quickly evacuated upon pumping down the system, thereby preventing virtual leaks. Depending on the quality of vacuum necessary to perform an experiment virtual leaks may or may not be of concern. However, because of the nature of virtual leaks, they are a constant source of increasing pressure inside of any vacuum system.

CHAPTER III: DIBS SYSTEM REPAIRS AND MODIFICATIONS

Although the main objective of this thesis research was to answer the question whether or not replacing the molecular oxygen during deposition with an atomic oxygen flux could improve the quality of ITO thin films deposited at room temperature, most of the time devoted to the project was to fixing the DIBS system. This section provides a short list of problems that were encountered and how they were addressed.

Repairs and Modifications

When this project was started the system had a base pressure of approximately 3x10^{-6} Torr. During deposition the water and nitrogen peaks measured by the RGA would slightly increase indicating a small leak in the substrate cooling system or the cooling system of the guns. The thermocouple gauge connected to the cryopump was also not functioning properly and the high vacuum gauge would not work in the 10^{-6} Torr range. Research by a previous student[20] showed that the properties of the ITO films made were very scattered and not always reproducible, particularly the effect of molecular or atomic oxygen. Additionally during the summer of 2012, the chain of the rotation mechanism of the sample holder broke and had to be replaced.

1. Gauges:

   (a) The broken thermocouple gauge attached to the cryopump was replaced with a Varian Eyesys Convectorr gauge. This gauge will take

measurements to pressures as low as 1x10^{-3} torr and allows for pressure curves to be measured to determine the outgassing rate of the switched off cryopump.

(b) The auto range of the high vacuum gauge was not working properly for the 10^{-6} torr range and required a thorough cleaning of the gauge using its degassing option. This indicated that the gauge had not been cleaned for sometime and/or a contamination of the vacuum system.

2. Vacuum Leaks: The vacuum was checked with helium gas as explained in the previous chapter. The following leaks were found:

(a) Several leaks were discovered on the sample-holder stage, including the feed through for the temperature sensor. These leaks were addressed when fixing the sample holder stage. In one of the feed throughs a rubber ring was missing. Another feed through appeared to have no option to include a rubber ring and had to be sealed with Teflon tape.

(b) In the tubing between the cryopump and the fore-line valve several leaks appeared over the course of three months. The tubes were connected by ISO-KF fittings which used a seal made out of an aluminum or stainless steel ring and a viton or silicon o-ring. Without out-baking they should remain operational to 10^{-7} torr. After cleaning seals with isopropanol alcohol and reassembling the system it was concluded that the cause of the leak was two fold: the high weight of the electronic valve between the cryopump and the roughing pump, and malfunctioning o-rings. The tubing layout was reconfigured to minimize the torque the heavy valve exerts on some of the KF connections. In the new setup the valve was supported by an adjustable platform and the number of fittings was reduced. All KF-fittings were sealed with a significant amount of high

vacuum grease to ensure that scratches on the flanges would not result in any small leaks. Additionally, the o-rings were replaced.

(c) In the ultra-high vacuum valve between the cryopump and the chamber, several leaks were found. Although some of the leaks were between the high pressure pneumatic and the vacuum chamber, they registered on the helium leak detector. All rubber rings and copper gaskets were replaced in the valve. This took several months since this valve is no longer in production and all rings had to be custom made.

(d) During the course of this project it was noticed that the RGA nitrogen peak increased when the compressed air was switched on. Switching on the air put $4.14 \text{x} 10^{3}$ torr of air on all pneumatic valves nearly instantaneously. This suggested that a leak existed between the high pressure pneumatic site of the system and the vacuum chamber. After further investigation, it was discovered that one of the pneumatic valves connected between the mass flow controllers and the system leaked directly into the vacuum chamber. The pneumatic valve was replaced. All unneeded gas lines and mass flow controllers except for the oxygen and argon lines were removed from the system.

(e) The pressure relief valve of the cryopump began leaking due to a bad spring and o-ring and was replaced.

3. Vacuum Pumps:

(a) The oil-sealed mechanical pump used to rough the chamber was removed from the system. Using the RGA, a peak referring to mechanical pump oil was found, indicating an oil contamination. It was discovered that the pump leaked oil on the floor of the laboratory and that the fore-line tubing was also contaminated with oil. The molecular sieve trap

currently in place was clearly not effective at preventing back streaming.

(b) The fore-lines of the chamber, the cryopump, and the turbo-pump were redesigned. The fore-line valve of the cryopump was removed and capped as it is possible to evacuate the cryopump through the chamber. A manual valve was inserted between the turbo pump and the scroll pump, allowing the scroll pump to be used for roughing the vacuum chamber.

(c) Before the Varian Tri-Scroll pump was used to rough the chamber, it was suggested by Eric Schires that it should be serviced. With his help, the pumps Teflon seals and bearings were replaced. Also the old seals had worn down and deposited dust into the pump and needed to be cleaned out with isopropanol.

4. Substrate Holder: The drive chain of the substrate holder broke in the beginning of the summer of 2012. The following modifications were made to the rotation stage:

(a) A new drive chain was purchased and installed. The whole sample holder had to be removed from the system and disassembled. When taking apart the sample stage it was discovered that several of the screws used in the stage did not have vent holes and would create a virtual leak as explained previously. Stainless steel screws with holes were ordered from McMaster Carr to reassemble the sample holder. The water channels, that use water to cool the sample holder, were found to be highly corroded. A vinegar solution did not prove effective, so the channels were submerged in RBS35 Detergent diluted with distilled water. This removed the majority of the corrosion. Furthermore, the flanges of the sample holder that sealed the cooling water part were damaged and a significant amount of high vacuum grease was needed to seal it. After reassembly, the RGA

water peak would no longer rise when the chiller was switched on.

(b) The thermal shields were deformed and damaged. The drive shaft of the rotator was resting on the shield and had reduced its thickness. The friction between the drive shaft and the shield most probably caused the drive chain to break. An attempt was made to replace the shield with a custom shield made by our technician, but had to be abandoned as Texas State currently does not have the welding expertise required for vacuum components. Several washers and a stronger spring were inserted in the sample holder so the shaft no longer touches the thermal shields. The old shields were placed back.

(c) When disassembling the sample holder it was discovered that one of the halogen heating lamps was broken and. The lamp was replaced.

5. Cleaning of the System: There were two indications of contamination within the vacuum system. A yellow powder was discovered on the grid of the main ion gun, and the high vacuum gauge required degassing after each pump down in order to achieve readings in the 10^{-7} torr range could be obtained. The following things were done to address those possible contamination issues:

(a) The inside of the system was carefully wiped with acetone followed by isopropanol. After this cleaning procedure it took almost a week before the high vacuum gauge would start showing values in the 10^{-7} Torr range again.

(b) The grid under the target holder between the chamber and the cryopump appeared to be corroded. It was replaced by a new stainless steel grid.

(c) After the replacement of the hot filament in the main ion gun, it was discovered that even at the optimal sputtering parameters that there was

no sputtering taking place. After it was determined that there was a problem with the internal components of the RF50 ion gun, it was removed and disassembled. Doing so revealed that the quartz discharge tube had been coated by a significant amount of the grid system when the argon beam had been backscattered. This was most likely caused by the accelerator grid becoming positively charged instead of negatively charged and driving the argon ions back into the discharge tube. the discharged tube was placed in a nitric acid bath for several days. Care was taken so that the metal coupling on the discharge tube did not come into contact with the acid because the acid is highly reactive with metals but not glass. Once the coating was removed from the tube, it was baked out at approximately 95°C to remove any excess water. It was then placed back into the gun and the ion gun began functioning properly again.

6. Cables and Control Electronics:

   (a) Most of the cables between the electronic equipment and the vacuum system were re-routed via the cable tray that extended from the ceiling. After this was done the PLC computer that controlled the pumps and valves connected to the system no longer worked. Resetting the PLC computer did not resolve the problem. After a careful investigation, two loose wires were found on the electronic boards in the back of the system. They were soldered back in the system.

   (b) To make it easier to manually adjust the impedance of the gun the power supply and control electronics of the assist gun were moved from the top of the instrument rack to a table adjacent to the sputtering system. This change allowed for easier adjustments to the settings on the gun in order

to reduce the reflected power. The table also changed the path around the equipment and provided protection for the cooling lines connected to the sample holder.

While repairing the system, few improvements in the base pressure of the system were observed. Significant improvements were noticed after the leaks in the pneumatic valve of the mass flow controller were sealed and after the high pressure relief valve of the cryopump was replaced. The system currently has a base pressure of 1.3x10^{-7} Torr (after several days of pumping).

The mono-layer formation time, i.e. the time required to form one mono-layer of gas atoms on a clean aluminum substrate (assuming a sticking coefficient of one) depends on the base pressure of the system and is given by:

$$\tau = \frac{2.4x10^{-5}}{P} \tag{3.1}$$

Where P is in Torr and τ in seconds. It is desired that the mono-layer formation time to be considerably larger than the oxygen flux (mono-layers per second) from the assist gun. As oxygen is the most important, the partial oxygen pressure should be used in the equation above. Assuming also that 20% of the residual gasses in the vacuum system is oxygen, the mono-layer formation time to be approximately 85 seconds. This results in a background oxygen flux of 0.01 mono-layer per second for the improved system. This is much smaller than the typical growth rate of the ITO samples (4 Å/second, 2 mono-layers per second) which suggested that the system was clean enough to do the experiments.

Another problem encountered with the DIBS system, was the erosion and the oxidation of the neutralizer filament of the main ion source. These processes can wear the filament down until it is thin enough to snap and needs to be replaced. Although replacing the filament is relatively simple, the process of removing the ion

gun from the system is somewhat lengthy and delicate - anything but the most careful of handling may damage the source tube in which the plasma is generated. After the ion gun is removed and the filament is replaced, one must make sure when it is replaced into the DIBS system that it is aligned properly. To perform this task, aluminum foil is placed around the target in the chamber. After evacuation of the chamber the ion gun is allowed to sputter through the foil. If successful, the beam location can be determined from the position of the hole in the foil. Adjustments can be made to the gun in order to change the beam direction. If the beam fails to punch a hole in the foil, then there is a connection problem with the wires in the grid assembly. In such case one should carefully check the connections to the rear of the gun.

When this experiment began the DIBS system was operational, but the system contained many unnecessary parts. Vacuum systems should always be as simple as possible to reduce the risk of any potential leak. The system was changed significantly over the course of the project. Figures 3.1 and 3.2 show diagrams of the DIBS system before and after modifications were made.

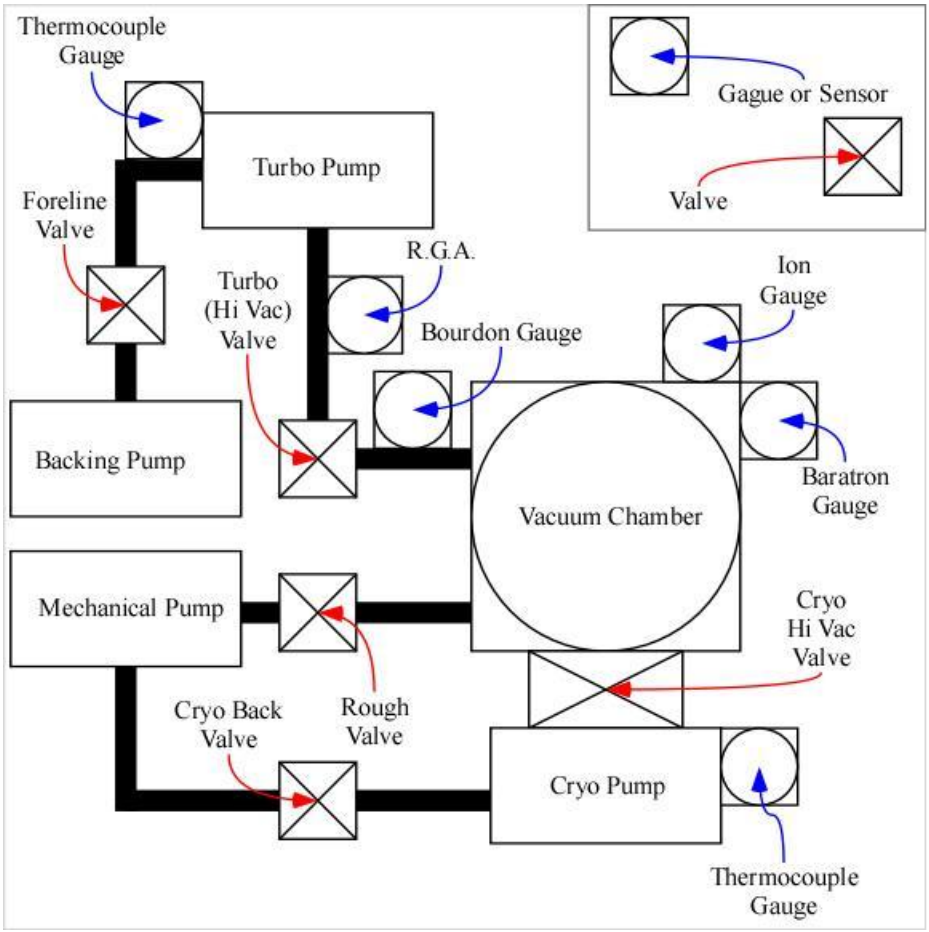

Figure 3.1: The DIBS System Diagram Before

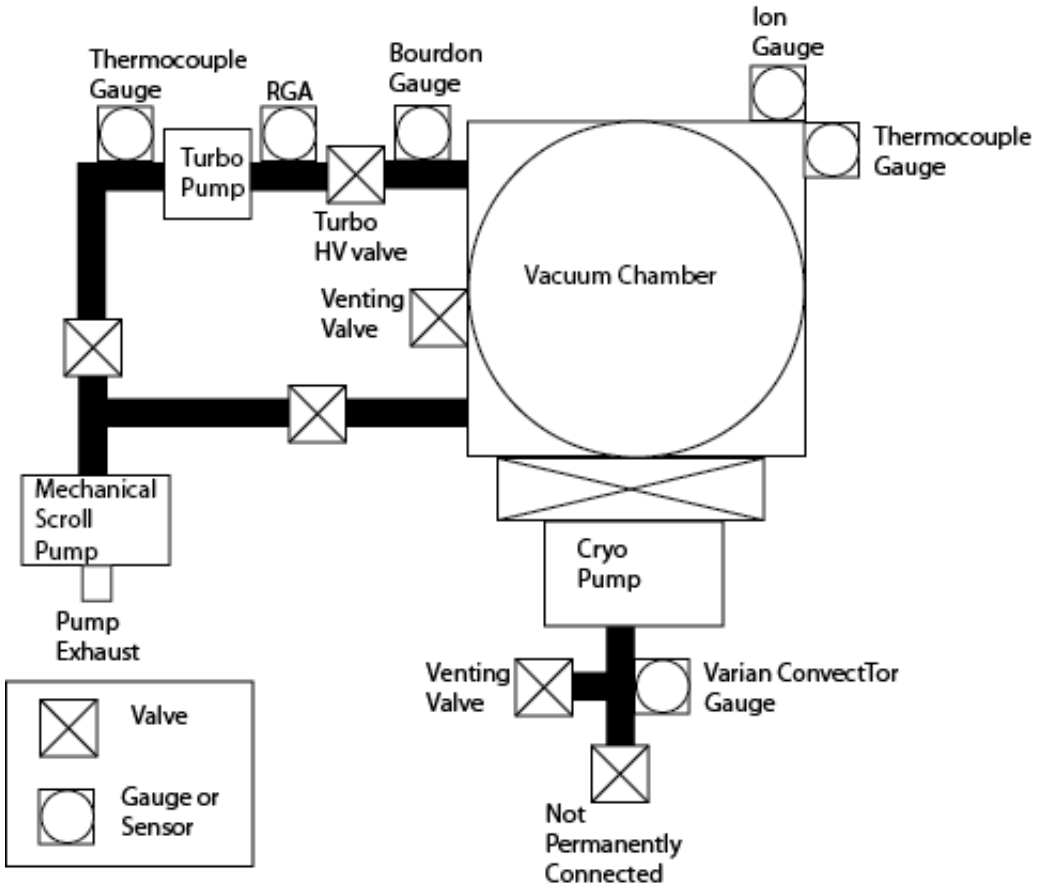

Figure 3.2: The DIBS System Diagram After

CHAPTER IV: SAMPLE SUBSTRATES

This chapter will describe the sample substrates that were used and how they were prepared prior to placement in the DIBS system.

Substrate Materials

The first substrate of choice was a glass substrate material, since the deposition of ITO occurs most commonly on glass substrates. For this material glass microscope slides from Carolina Biological Supply Company were used. The slides are made from soda-lime glass, have precision-ground edges, and were annealed by the manufacturer to minimize chipping and breaking. They measure 25 x 75 mm and have a thickness of 0.96-1.06 mm.[21]

Soda lime glass consists of mainly SiO_2, i.e. fuzed quartz. To lower the glass transition temperature the manufacturer adds Na_2CO_3 to the melt. However the soda makes the glass soluble in water, so to improve the chemical durability CaO (lime), MgO, and Al_2O_3 are added to the glass. Approximately 90% of all manufactured glass is soda lime glass. Glass sheets are normally made by floating molten glass on a bed of molten metal. This results in very flat sheets of glass with a homogeneous film thickness. Typically tin is used for this process. To avoid the adhesion of SnO_2, the procedure normally takes place in an atmosphere of N_2 and H_2. The glass panels used for photovoltaics are normally low iron float glass which has a slightly higher transmittance than standard soda lime glass.

The other material that was used as a substrate was [100] n-type silicon

(sheet resistance 2.39x10^2 Ω/□). The silicon wafers had a native oxide of approximately 2nm. The samples for deposition were cut from 4 inch wafers.

Substrate Cleaning Procedure

To prepare the samples for placement into the DIBS system, the samples were thoroughly cleaned using an VWR Scientific Aquasonic Model 250D ultrasonic cleaner. The purpose of the cleaning was to ensure that the samples were clean and free of contaminates that could cause defects or ultimately negatively affect the composition of the deposited films.

All substrates started their cleaning process with a quick rinse with isopropyl alcohol to rinse any large particles, such as dust, from the surface. The glass substrates were submerged in an acetone bath and cleaned ultrasonically for five minutes, then rinsed again with isopropyl to remove any acetone residue. Both the glass slides as well as the silicon samples were submerged in an isopropyl bath and cleaned ultrasonically for five minutes, then dried using compressed pure nitrogen gas. Then, the substrates were placed into the DIBS machine for deposition.

CHAPTER V: DEPOSITION METHOD

The preparation of thin films by methods involving the assistance of the film growth with accelerated ion species can be carried out using several approaches. Different methods can be considered depending on the procedure utilized for providing the material to be deposited and how the ions are generated, accelerated and directed towards the substrate.[22] This chapter will detail how the samples were made for this experiment and will discuss the process of Ion Beam sputtering.

Thin Film Growth Process

A thin film is a layer of material ranging from fractions of a nanometer to several micrometers in thickness. These films have found application in electronic devices, optical coatings and decorative parts. Thin films are also necessary for the development of hard coatings and wear resistant films. The act of applying a thin film to a surface is referred to as thin-film deposition. "Thin" is a relative term, but most deposition techniques control layer thickness within a few tens of nanometers.

Deposition techniques fall into two broad categories, depending on whether the process is primarily chemical or physical. Within each category exist several types of deposition, as noted in Table 5.1. Any thin film deposition method involves three main steps: (1) production of the appropriate atomic, molecular, or ionic species, (2) transport of these species to the substrate through a medium, (3) condensation on the substrate, either directly or via a chemical reaction, to form a solid deposit.

Table 5.1: **Methods of Film Deposition and their Types**

Chemical Deposition	Chemical Vapor Deposition
	Spin Coating
	Plating
Physical Deposition	Sputtering
	Molecular Beam Epitaxy
	Pulsed Laser Deposition

Thin films can be generated by nucleation and growth processes which can be described as follows:[23]

1. The species, upon impacting the substrate, lose their velocity component normal to the substrate and become physically absorbed on the substrate surface.

2. These absorbed species are allowed to move over the surface of the substrate and can interact with other absorbed species, forming bigger clusters, because they are not in thermal equilibrium.

3. The newly formed clusters are still not in thermal equilibrium and tend to desorb from the substrate. Under the right conditions, clusters might combine with other clusters. These larger clusters eventually reach a critical size and become thermodynamically stable; this is called the nucleation stage.

4. The clusters continue to grow in size and number until a saturation density is reached. This density depends on a number of conditions including, but not limited to, the energy of the impinging species, the rate of impingement, the activation energies of absorption, desorption, the temperature, and chemical nature of the substrate. A cluster, or nucleus, has the possibility to grow both parallel and perpendicular to the substrate.

5. When the saturation density is reached, the nuclei begin to coalesce together in an attempt to reduce the surface area. This is referred to as agglomeration

and can be enhanced by increasing the mobility of the surface species. New nuclei can then be formed on the newly exposed substrate.

6. Larger nuclei grow together, leaving channels and holes of uncovered substrate. This type of film is very porous and discontinuous. A completely continuous film is achieved by filling these channels and holes.

7. For reactive sputtering of oxide thin films, oxygen molecules arriving at the substrate will react with the already deposited atoms. For an oxygen molecule to be incorporated in the substrate its oxygen bond needs to be broken which requires a certain amount of energy. It is expected that higher substrate temperatures will make it easier for this to happen.

This growth process then can be summarized as multiple statistical processes beginning with nucleation, then surface controlled growth of the nuclei, and the formation of a network structure that subsequently fills to form a continuous film.

Principles of Dual Ion Bream Sputtering

For this experiment a physical deposition process called sputtering was used to deposit the ITO films. Sputtering occurs when a solid surface, or the target, is bombarded with energetic particles, i.e. ions, and the surface atoms of the target are scattered outward due to the collisions between the high energetic incident ions and the atoms of the target. This process can be seen in Figure 5.1. There are many different types of sputtering methods, including magnetron, radio frequency, ion-beam, and reactive sputtering. All of these techniques allow for the deposition of materials with very high melting points and create films that have an almost identical composition to that of the target material. Sputtered films typically have a better adhesion on the substrate than evaporated films. Sputtering also has its

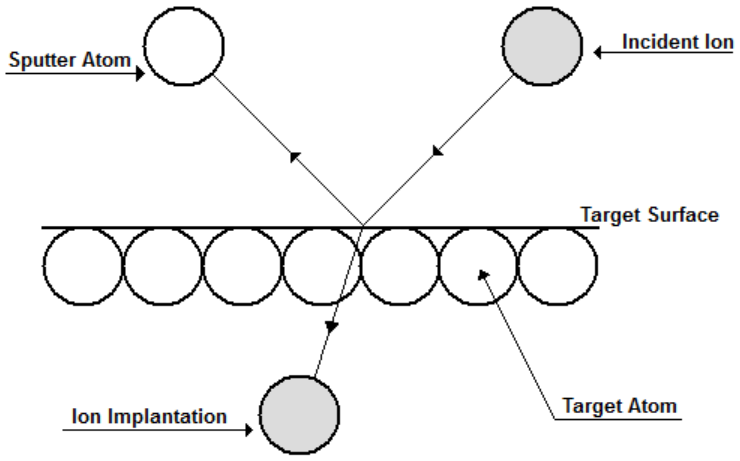

Figure 5.1: Physical Sputtering Process

disadvantages. During sputtering,the atom's movement cannot be fully restricted, which can lead to contamination in the sample and chamber. Also, controlling layer-by-layer growth is extremely difficult because the inert sputtering gases are built into the film as it grows.

For this experiment an ion-beam sputtering system was used. The plasma was contained in the gun and was not in direct contact with the substrate, allowing for deposition at much lower temperatures. The ion beam sputtering system was manufactured by Commonwealth Scientific Corporation and has been modified to use two different ion sources, hence the name dual ion beam sputtering system. In the DIBS system, the sputtered material was deposited on the surface of the substrate while, simultaneously, the growing film was bombarded with ions or atoms from the second source. A schematic of the geometry of the system can be seen in Figure 5.2.

The DIBS system has a few critical geometrical restrictions that refer to the relative orientation of the target and the substrate positions. The geometrical arrangement of both elements has to be taken into account to understand the spatial distribution of atoms sputtered from the target. The amount of material

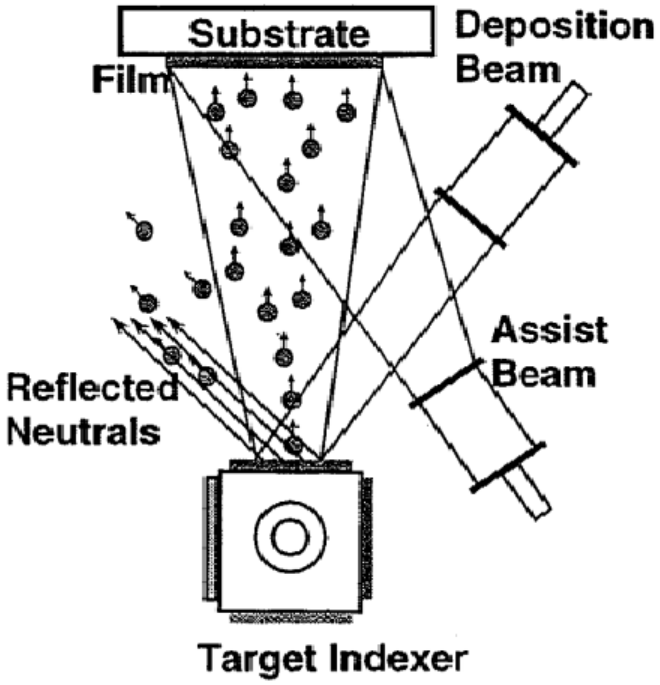

Figure 5.2: DIBS System Geometry

sputtered from a given target roughly follows a cosine distribution function with respect to the normal of the target. Therefore, to achieve a uniform distribution of the sputtered material on the substrate, the substrate must be located at a tangents position with respect to a spherical curve defined by this cosine distribution function.[22] For this reason, the major portions of DIBS systems are designed to keep the substrate and the target parallel to each other. To insure a homogeneous film growth, the substrate was also rotated at a uniform, and controllable rate. It was also important that the ion or atom flux of the assist beam be homogeneous across the surface of the sample. Another geometrical restriction of DIBS is the angle between the assist ion beam and the substrate. Changing this angle allows for greater control of the film's texture.

Typically, the ion source used for material removal by sputtering operates at relatively high energies to maximize the sputtering yield, which is given by equation

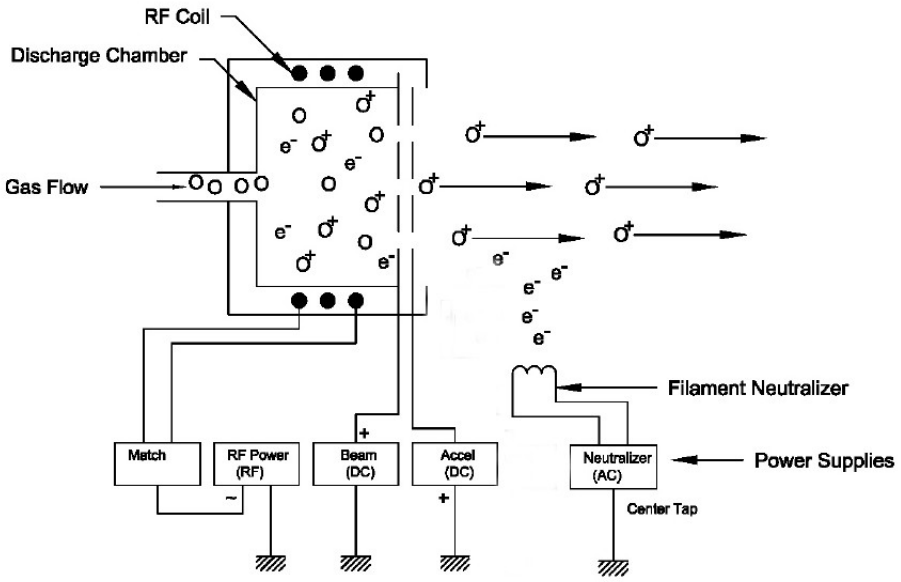

Figure 5.3: Schematic of Ion Source Gun

5.1 and describes the removal rate of surface atoms due to ion bombardment.[23]

$$S = \frac{atoms\ removed}{incident\ ions} \tag{5.1}$$

The assist gun will usually operate at lower energies to limit the damage of the impinging atoms. The main gun used for sputtering in this project was an Oxford Applied Research RF50 RF ion source that used argon as a sputter gas. It was directed at an angle of 45 degrees with respect to the target. This geometry guaranteed that the high energy argon atoms that were elastically and inelastically reflected from the target were not be incident on the substrate. The assist gun was an Oxford Applied Research HD25 RF atomic source, supplied with O_2 gas.

Both the RF50 ion and the HD25 atomic sources are considered Kaufmann type ion sources. This type of ion source is now the most widely used ion source in the thin film industry. A basic schematic of this type of source can be seen in Figure 5.3. The basic elements of this source are a plasma source, either electrode or RF sources, a grid system that separates the source from the chamber, and a neutralizer

filament.[22]

Both the RF50 and HD25 sources employ a RF coil to generate their plasma. An RF plasma is formed in a vacuum of 10^{-3} torr when exposed to RF electro-magnetic waves of a few hundred watts. The RF waves have a frequency that can vary from a megahertz to tens of megahertz; the DIBS system for this project operated at 13.56 MHz. There are two ways in which a gas can be excited by RF voltages: (1) capacitively coupled plasma and (2) inductively coupled plasma. The majority of RF ion sources used in the semiconductor industry are operated with the second type of plasma. This type of plasma is induced by an induction coil which generates an azimuthal RF electric field by the alternating magnetic field in the discharge tube. The electrons that are present in the gas volume begin to oscillate according to the RF electric field. While oscillating, these electrons quickly acquire enough kinetic energy to form a plasma by ionizing the background gas particles.[24,25]

These ions are extracted from the discharge tube by the grid system. This grid system consists of a screen grid, which is in direct contact with the plasma, and an accelerator grid separated from the screen by a few millimeters. The positively charged screen grid is typically kept at approximately 850 volts. As the ions slowly pass through the holes of the screen grid, they are then pulled towards the negatively charged accelerator grid, hence the name. The alignment of the two grids is extremely important, because for the ions to leave the gun and sputter the target material the holes of the grids must line up almost perfectly. If they are not then the ions will sputter the grid material instead of the target. An optical microscope can be used to verify proper grid alignment. With the holes in alignment, the low energy ions will flow through the screen grid unobstructed and will be accelerated toward the accelerator grid. The ion beam is formed by the sum of the individual

beamlets produced by each hole of the grid system. Once the ions have left the gun they are neutralized by a hot tungsten filament spanning the accelerator grid just outside the gun. The total beam diameter will approach the diameter of the grids, although it may become broader if not properly neutralized by the filament.[22] This neutralizing filament produces electrons to compensate for the positive charge of the ions coming out of the grid system. This helps to avoid the generation of undesired charging voltages at the target that might repulse the incoming ions and alter their kinetic energy.

An important operating parameter of an ion source is the ion-current density. This current density is caused by the electric potential that is applied across the grid system. The I-V characteristic of an ion source is limited by a Child-Langmuir equation resulting in a non-linear I-V relation. This limitation is caused when moving ions pass through the screen grid and positive space charges build up near the grid and slow down further positive charge injection until these positive charges are removed by the accelerator grid. The I-V relation of an ion gun is given by:

$$J_+ = K\left(\frac{q}{m}\right)^{\frac{1}{2}}\left(\frac{V_t^{\frac{3}{2}}}{S^2}\right) \tag{5.2}$$

where q and m denote the electronic charge and the mass of the ions, respectively; V_t denotes the voltage difference between the grid system; S is the spacing between the two grids; and K is a constant. For a grid system with parallel grids, K is expressed by equation:

$$K = 4\left(\frac{e_0}{9}\right) \tag{5.3}$$

where e_0 denotes the transmission rate of the grids.[26] From equations 5.2 and 5.3, it is clear that the smaller the distance between the grids and the larger V_t becomes the larger the current density will be. A higher V_t means that the energies of individual ions will increase, which is undesirable in certain applications.

The HD25 atomic source operates a bit differently than the RF50 ion source in that the atomic source does not use an accelerator grid to accelerate the ions to the sample. It has been shown by others that high energetic ions incident on the film during deposition can cause point defects in the thin ITO film and negatively impact the mobility of the electrons, resulting in a higher resistivity.[5,7–10] Therefore, acceleration is not desirable for the assist gun. The energy of the atoms coming from the HD25 gun is lower than 50 eV and is not believed to cause such point defects. Compared to the energy (up to 1 KeV) of the high momentum ions from the main ion source, the atoms coming out of the assist gun have a much lower momentum. The low energy of the atom beam of the HD25 was confirmed by an experiment in which a silicon wafer covered with a thin native oxide film was exposed to an oxygen beam from the HD25 for twenty minutes. The increase of the native oxygen layer thickness as measured by spectroscopic ellipsometry was less than 1.5 Angstroms. The atomic source also does not use a neutralizer filament but employs an ion deflection plate. This plate deflects any ions that are created by the plasma and allows only the atomic and molecular neutral particles to pass onto the sample. Although there is no good way to determine the relative ratio of atomic to molecular oxygen provided by the assist beam, information provided by Oxford Applied Research suggests that typical efficiencies of atomic sources are close to 60%.

For a proper control of the process parameters for deposition using the DIBS system, the gas flow, the RF energy of both sources, and the acceleration and screen voltages for the RF50 must be very carefully adjusted. The amount of material supplied to the substrate for film growth depends strongly on the ion energy and density of the main ion gun. Meanwhile, any modifications to the film characteristics are produced by adjusting the same parameters for the assist gun, HD25. Also, by adjusting the oxygen flow in the assist gun, the stoichiometry of oxides grown by DIBS can be controlled. Strict control of these parameters allows

the quality of films prepared by DIBS, in terms of low roughness and high adherence to the substrate, to be very good.[18]

Sputtering by dual ion beams provides many advantages. These include the fact that the sample is not directly in contact with the plasma. This allows for films to be deposited at much lower temperatures, even room temperature. Since the plasma is contained in the guns discharge tube, sputtering can be performed at lower system pressures, allowing for a wider process window. Also, the incident angle of the ion guns are controllable, so ion energy is controlled independent of working pressure. Ion current density is controllable by either ion energy or gas pressure. It allows for dense smooth films, minimal optical losses, and excellent uniformity. With regards to the characteristics, DIBS is a very well suited technique for the deposition of films for optical application and high corrosion protection. Because of this DIBS deposition allows for a highly successful run-to-run process and quality repeatability.[22,25,26]

However, the DIBS technique is not with out drawbacks. Since sputtering is usually less effective than other deposition methods such as evaporation, the growth rates achieved by DIBS are, in practice, lower than those obtained by other physical deposition methods. During the deposition of the samples used for this project, the temperature of the main ion source increased dramatically mainly due to the filament. This increased temperature increases the outgassing of the gun parts and increases the effective base pressure of our system. Leaving the gun at this elevated temperature level could damage the components of the ion gun. Therefore, deposition time was limited to twenty minute sessions.[18,22]

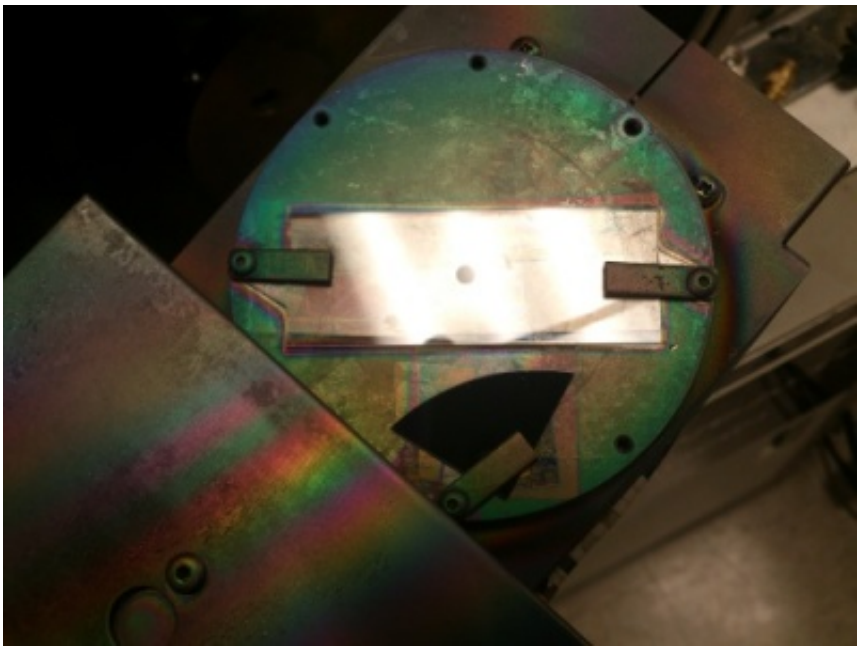

Figure 5.4: Placement of Sample on Sample Stage

Placement of the Sample in the Chamber

To hold the substrate in the chamber for deposition, the substrate was placed on the sample holder. The sample holder was a flat, circular disk, that had clips on the edge that were used to hold the substrate flush with it surface to guarantee good thermal contact. As seen in Figure 5.4, these clips are tightened using hex bolts. Caution was taken when tightening these bolts so as not to crack or break the substrates. Another reason to not over tighten these bolts is so that the samples did not break during deposition. While sputtering, the sample might heat slightly and if the pressure of the clips are just right, the samples might crack or break.

Figure 5.4 shows the placement of the silicon and glass substrates. The glass slide was considered the more important substrate for this experiment, therefore it was centered on the sample holder and secured by two clips. The silicon substrate was then placed on the side of the glass side and secured by one clip. With the size of the silicon samples, care was taken to ensure that the clip held the sample

securely but still allowed for the maximum unobstructed surface for deposition.

Deposition Parameters

All of the samples used in this experiment were deposited under the conditions outlined in table 5.2. An ITO target having a composition of 90% wt. In_2O_3 ans 10% wt. SnO_2 and a purity of 99.99% was used for all ITO samples. A few parameters are not included in the table because they were set and did not change at all during the entire sample series. These parameters include the neutralizer filament current and the currents of the screen and accelerator grids. The filament current was placed at 5 amps for each run and process. This value was chosen such that it was certain that the filament current was larger than the beam current in order to reduce surface charging at the target. The screen grid and accelerator grid currents were operated in between 56 to 60 milliampere and 6 to 7 milliampere respectively. This setting(an accelerator grid to screen grid current ratio of approximately 0.11-0.12) provides a good quality grid focusing.[18]

Table 5.2: **Deposition Parameters**

Sample Number	031613A	032013P	032513P	032713A	032813A	040113P	040313P	040413P	040913P	041513P	041813A	041913A	042313P
Base Pressure (torr)	$2.60x10^{-7}$	N/A	$3.00x10^{-7}$	$3.00x10^{-7}$	$3.20x10^{-7}$	$1.20x10^{-7}$	$3.00x10^{-7}$	$2.60x10^{-7}$	$1.60x10^{-7}$	$3.30x10^{-7}$	$1.90x10^{-7}$	$2.80x10^{-7}$	$3.00x10^{-7}$
Argon Flow (sccm)	15	15	15	15	15	15	15	15	15	15	15	15	15
SiO_2 Buffer Layer													
Assist On/Off	Off	On	On	On	On	On	On	On	On	On	On	On	On
Pre-Sputter Time (min)	5	5	5	5	5	5	5	5	5	5	5	5	5
Sputter Time (min)	20	20	4	4	4	4	4	4	4	4	4	4	4
O_2 Flow (sccm)	7	4	4	4	4	4	4	4	4	4	4	4	4
Operating Pressure (torr)	$7.40x10^{-4}$	$6.80x10^{-4}$	N/A	$7.00x10^{-4}$	$7.00x10^{-4}$	$7.40x10^{-4}$	$7.00x10^{-4}$	$7.20x10^{-4}$	$7.40x10^{-4}$	$7.00x10^{-4}$	$7.40x10^{-4}$	$7.40x10^{-4}$	$7.20x10^{-4}$
Main Gun Power (Watt)	80	80	80	80	80	80	80	80	80	80	80	80	80
Assist Gun Power (Watt)	-	211	210	208	209	210	210	211	208	205	208	207	206
Assist Gun Intensity (a.u.)	-	0.121	0.120	0.118	0.118	0.122	0.121	0.121	0.120	0.119	0.121	0.119	0.120
ITO Layer													
Assist On/Off	-	-	Off	On	-	Off	On	Off	On	Off	On	Off	On
Pre-Sputter Time (min)	-	-	5	5	-	5	5	5	5	5	5	5	5
Sputter Time (min)	-	-	20	20	-	20	20	20	20	20	20	20	20
O_2 Flow (sccm)	-	-	1	1	-	2	2	3	3	4	4	5	5
Operating Pressure (torr)	-	-	$7.00x10^{-4}$	$6.80x10^{-4}$	-	$7.00x10^{-4}$	$7.00x10^{-4}$	$7.10x10^{-4}$	$7.40x10^{-4}$	$7.40x10^{-4}$	$7.40x10^{-4}$	$7.40x10^{-4}$	$7.40x10^{-4}$
Main Gun Power (Watt)	-	-	80	80	-	80	80	80	80	80	80	80	80
Assist Gun Power (Watt)	-	-	-	216	-	-	212	-	205	-	209	-	205
Assist Gun Intensity (a.u.)	-	-	-	0.086	-	-	0.116	-	0.118	-	0.123	-	0.115

When the experiment first started it was known from background research that groups were using an SiO_2 buffer layer to allow the ITO to better adhere to the glass substrate and to avoid possible issues with sodium leaking out of the glass substrate (see Chapter IV). From this, it was decided to deposit a thin layer of SiO_2 before the ITO deposition. The assist gun, at an O_2 flow rate of 4 sccm, was used for all SiO_2 depositions.

The HD25 atomic source can provide a plasma and atomic particles at a flow rate from 1-10 sccm. The intensity of the plasma varies as a function of the flow rate and the supplied RF power. An optical detector is installed on the HD25 gun that monitors the intensity of the plasma. This intensity provides an insight into the efficiency of the source. At optimal conditions the source operates at about 60% efficiency which means that 60% of the flux is atomic particles. To optimize the intensity the RF power of the source and the gas flow rate need to be balanced. These parameters can be varied to achieve the maximum efficiency of the source. In general, the atomic content of the beam will increase nearly linearly with the power, while the relationship with the gas flow is more complex. Varying the RF power and gas flow rate and recording the intensity values provided Figures 5.5 and 5.6. From these figures it was decided that an O_2 flow rate of 4 sccm and a RF power of approximately 200 Watts would provide the most efficient use of the atomic source.

The power for the main ion gun was set at 80 watts to insure that proper sputtering of the target would take place and still minimize to possibility of sputtering the target holder. An early sputtering session indicated that at higher RF power levels (100-110 Watts) and for poor alignment of the main ion gun, the target would heat up too much such that the indium bonding of the ITO to the copper back plate would melt. Therefore it was decided to keep the RF power for this project at 80 Watts to prevent this from happening again.

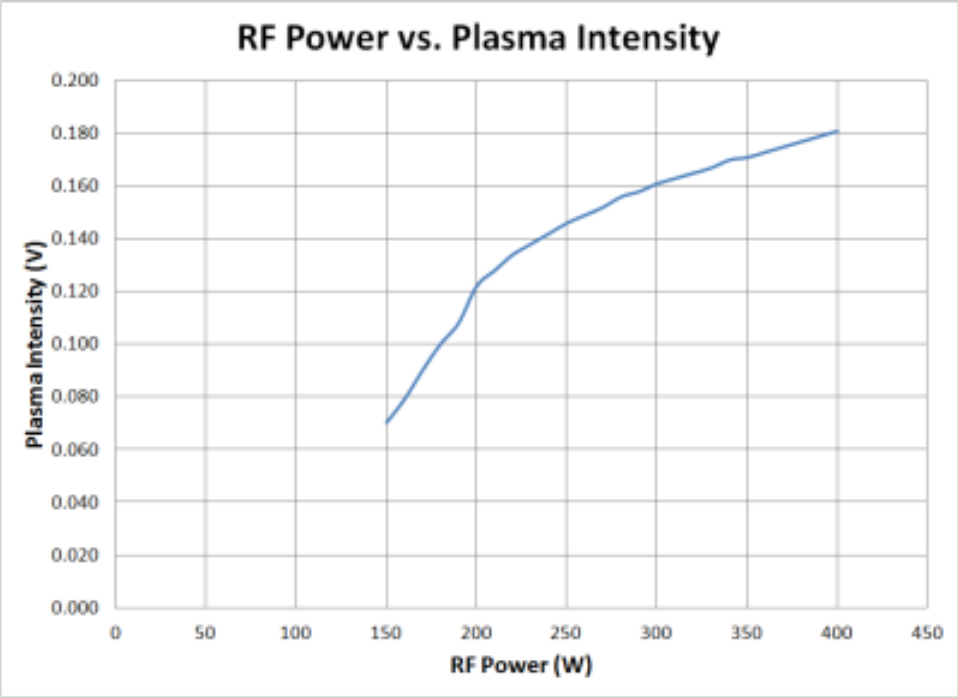

Figure 5.5: Relationship Between RF Power and Plasma Intensity

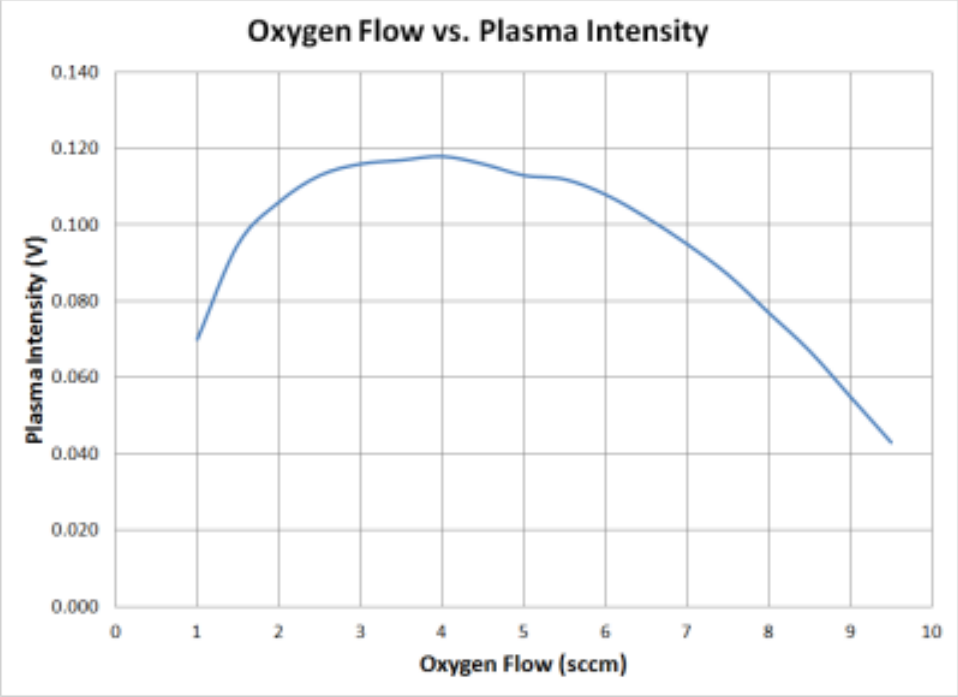

Figure 5.6: Relationship Between O_2 Flow Rate and Plasma Intensity

CHAPTER VI: ELLIPSOMETRY

To characterize the samples that were produced by DIBS, a J.A. Woollam Ellipsometer, supplied by Dr. Droopad, was used to provide spectroscopic ellipsometric data. From this we can determine film thickness and optical properties, such as the index of refraction and the absorption coefficient. This chapter will provide a background to ellipsometry and discuss measurement parameters used to characterize the samples.

Theory of Ellipsometry

Ellipsometry is a contactless, non-invasive technique measuring changes in the polarization state of light reflected from a surface. It deals with intensity-dependent complex quantities compared to intensities for reflectance or transmittance measurements. Ellipsometry is considered an impedance measurement, while reflectance or transmittance are power measurements. Impedance measurements give the amplitude and phase, whereas power measurements only give amplitudes. One determines the complex reflection coefficient ratio of the sample that depends on the ratio of the complex reflection coefficient for light polarized parallel and perpendicular to the plane of incidence.[27]

Light and polarization are integral components of ellipsometry. Light waves are electromagnetic waves traveling through space and the electric field is always orthogonal to the propagation direction. Therefore, a wave traveling along the z-direction can be described by its x- and y- components. Most light sources emit light that has components with electric fields oriented in all possible directions,

known as unpolarized light. When the electric field vector of an EM wave only has a component in a specific direction, the light is referred to as polarized light, or more commonly known as linearly polarized light. Linearly polarized light can be considered to consist of two orthogonal linearly polarized waves that are in phase with each other. There are two other types of polarized light, circularly (out of phase by 90°) and elliptically (a phase difference other than 90°) polarized light. The later type of polarization is the most common and is where ellipsometry receives its name.

When light interacts with a material of any kind two phenomena occur. The light is either reflected away from the material or transmitted through the material. When light is transmitted through a material, there are two values which are used to describe the light's interaction with a material, the index of refraction, n, and the extinction coefficient. These values are usually defined as a complex number called the complex index of refraction, which is defined as:

$$\tilde{N} = n - ik \tag{6.1}$$

When light is traveling through air, its speed is close to that of the speed of light in a vacuum, 3x10$^8 m/sec$. However, when light is traveling through a material, it's speed is significantly different. Therefore the index of refraction, n, is defined as:

$$n = \frac{c}{v} \tag{6.2}$$

Where c is the velocity of light in air and v is the velocity of the light through the material. This means that the index of refraction for air is close to 1.[28,29]

The extinction coefficient, k, describes the loss of wave energy in the material and is related to the absorption coefficient, α, which must be considered first. In an

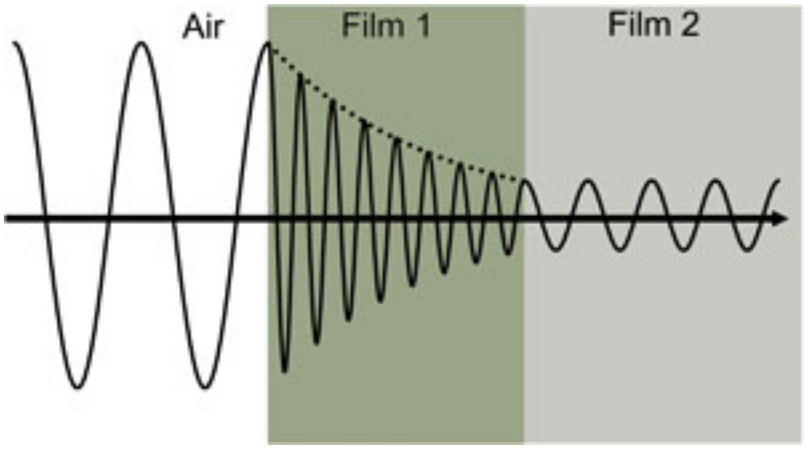

Figure 6.1: When a light wave becomes incident on an absorbing film, Film 1, its intensity and wavelength begin to decrease as it travels through the film. When the wave reaches the transparent film, Film 2, the light undergoes another velocity change.[29]

absorbing material, the decrease in the lights intensity per unit length z is proportional to the value of the intensity, providing the following differential equation:

$$\frac{dI(z)}{dx} = -\alpha I(z) \tag{6.3}$$

The solution to this equation is:

$$I(z) = I_o e^{-\alpha z} \tag{6.4}$$

Where I_o is the value of the intensity at the surface of the absorbing medium and α is the absorption coefficient in cm^{-1}. The extinction coefficient is related to the absorption coefficient through the following relation and is dimensionless:

$$k = \frac{\lambda}{4\pi}\alpha \tag{6.5}$$

Where λ is the wavelength of the light. Therefore, the extinction coefficient relates to how quickly light vanishes in a material. These properties are illustrated in Figure 6.1.

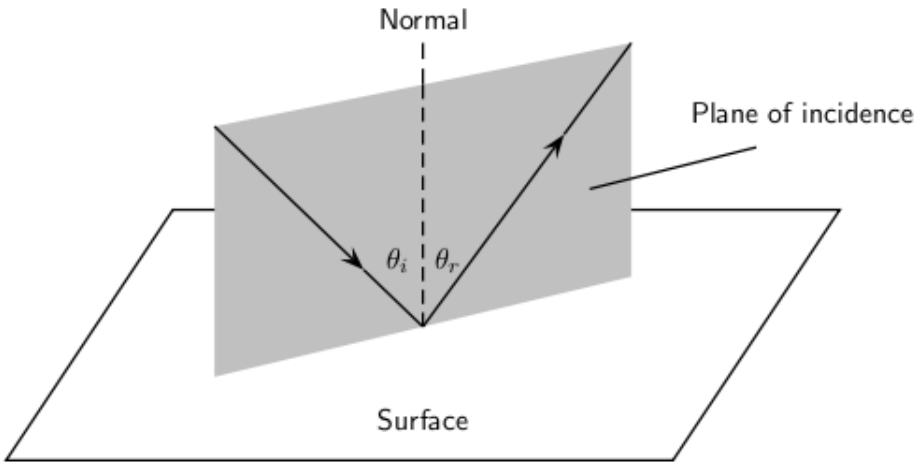

Figure 6.2: The Plane of Incidence during Reflection of Light

When the light becomes incident on a flat surface with the material, some of the light is reflected and the rest is refracted according to Snells Law. The portion that is reflected defines a plane of incidence that contains the incident light beam, the reflected beam, and the surface normal as shown in Figure 6.2.

The waves that are polarized parallel to the plane of incidence are referred to as "p-waves" and the waves that are polarized perpendicular to the plane of incidence as "s-waves". For an isotropic material the electric fields of the reflected wave are completely independent of each other and can be calculated separately using Maxwell's equations. This derivation results in the the Fresnel relationships, that express the ratio of the electric field before and after reflection and are given by the following expressions:

$$r_{12}^{s} = \left(\frac{E_{o_r}}{E_{o_i}}\right)_s = \frac{n_1 cos(\alpha) - n_2 cos(\beta)}{n_1 cos(\alpha) + n_2 cos(\beta)} \tag{6.6}$$

$$r_{12}^{p} = \left(\frac{E_{o_r}}{E_{o_i}}\right)_p = \frac{n_2 cos(\alpha) - n_1 cos(\beta)}{n_1 cos(\beta) + n_2 cos(\alpha)} \tag{6.7}$$

$$t_{12}^{s} = \left(\frac{E_{o_t}}{E_{o_i}}\right)_s = \frac{2n_1 cos(\alpha)}{n_1 cos(\alpha) + n_2 cos(\beta)} \tag{6.8}$$

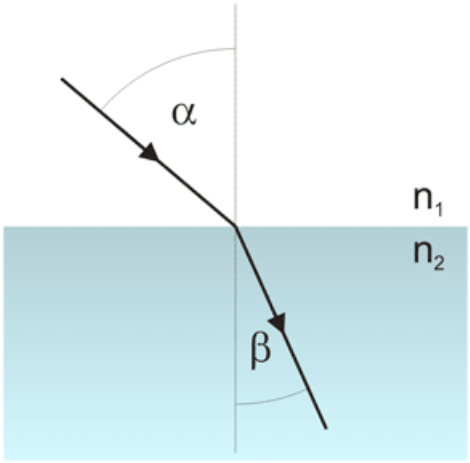

Figure 6.3: A Light Wave Interacting at a Boundary of two Materials

$$t_{12}^{p} = \left(\frac{E_{o_t}}{E_{o_i}}\right)_p = \frac{2n_1 cos(\alpha)}{n_1 cos(\beta) + n_2 cos(\alpha)} \tag{6.9}$$

Where α, β, n_1, and n_2 are defined in Figure 6.3.

Note that since the refraction index is complex the Fresnel reflection and transmission coefficient are in general also complex. Their magnitude represents the ratio of the reflected (transmitted) and incident light amplitudes. Their argument demonstrates the phase shift of the EM wave upon reflection and or transmission. Although ellipsometry can be done in reflection or transmission, the Woollam ellipsometer only allows for reflection measurements.[28,29] Thin film and multilayer structures involve multiple interfaces, with Fresnel reflection and transmission coefficients applicable at each. It is important to track the relative phase of each light component to determine correctly the overall reflected or transmitted beam. For a thin film on a bulk substrate the total Fresnel reflection coefficients can be calculated from:

$$R^s = \frac{r_{12}^s + r_{23}^s e^{-i2\phi}}{1 + r_{12}^s + r_{23}^s e^{-i2\phi}} \tag{6.10}$$

$$R^p = \frac{r_{12}^p + r_{23}^p e^{-i2\phi}}{1 + r_{12}^p + r_{23}^p e^{-i2\phi}} \tag{6.11}$$

Where the subscripts denote the coefficients for the interface between those two

mediums and ϕ, here is defined as:

$$\phi = 2\pi \frac{d}{\lambda} n_2 cos(\beta) \tag{6.12}$$

where d is the film thickness.

Ellipsometry primarily demonstrates how p- and s- components change upon reflection in relation to each other. Therefore the values, Ψ and Δ, are defined and are the most commonly used variables in ellipsometry.[27] Delta, is defined as the change in phase difference between the s- and p- waves of the light upon reflection. Assume δ_1, to be the phase difference between the p and s components of the incident wave and δ_2 to be the phase difference between the p and s components of the reflected wave. The quantity Δ is defined as:

$$\Delta = \delta_1 - \delta_2 \tag{6.13}$$

Delta's value ranges from zero to 360°. Psi is defined in such a way that it is the angle whose tangent is the ratio of the magnitudes of the total reflection coefficients, such as:

$$tan\Psi = \frac{|r^p|}{|r^s|} \tag{6.14}$$

Psi's values ranges from zero and 90°. With these two parameters known, under some conditions the film thickness, refractive index, surface roughness, and/or uniformity can be calculated.

Equations 6.13 and 6.14 can be summarized as:

$$tan(\Psi)e^{i\Delta} = \frac{r^p}{r^s} = \rho_{ellipsometry} \tag{6.15}$$

J.A. Woollam Ellipsometer

Ellipsometry is a well respected technique for studying surfaces and thin films. A wide array of different ellipsometer configurations exist including the rotating analyzer (RAE), the rotating polarizer (RPE), the rotating compensator (RCE), and the phase modulation (PME) configuration.

A common application of the afore mentioned ellipsometry configurations is in film thickness measurements. But it can also be used for other applications, because the ellipsometric angles Ψ and Δ are sensitive not only to layer thickness, but also depends on optical constants of the sample surface, which are strongly related to composition, microstructure, and surface condition of the sample. Spectroscopic ellipsometric(SE) measurements have extended the range of ellipsometry by using more than one wavelength. Furthermore, it is possible to vary not only the wavelength but also the angle of incidence, providing yet another degree of freedom. This allows non-invasive, real-time process measurements such as layer growth monitoring during MBE. Variable wavelength and angle allows optimization for a material parameter of interest, something that is not usually possible with fixed-angle, constant-wavelength ellipsometry. It also provides additional measurement values and allow for more than two unknowns to be determined from the measured spectra.

The ellipsometer that was used for this project is a J.A. Woollam M2000 variable angle spectroscopic ellipsometer. It is a very powerful tool for characterization of thin films. Under appropriate circumstances, SE has the possibility to measure film thickness better than any other known method, with resolutions in the submonolayer range.[30] However, the data measured by SE is usually not very interesting within itself. The more useful and important information, i.e. film thickness and optical properties, can only be determined by

the modeling of the surface region of the sample and then fitting the SE data to the model using the desired parameters as variables in the numerical analysis. Clearly, the way the fit and analysis is preformed is crucial, and inappropriate modeling of the results can often lead to worthless results.

Measurement Parameters

The operation of the Woollam ellipsometer is straight forward. After powering up the ellipsometer and it is allowed to calibrate itself, the sample to be measured is placed on the sample stage. Then the measurement parameters for the run are chosen. These parameters include, what angles the light is incident at, integration time, wavelength range, and measurement mode. For each sample, the measurements were taken at 5 different angles, 50-70° in 5° increments, over the entire possible spectral range of the instrument(200-1000nm), with an integration time of three seconds in reflection mode. For the samples that were deposited onto the glass substrates, transmission measurements were taken in transmission mode. This mode places the ellipsometer at a 90° angle of incidence and allows for the light to be directed through a sample placed perpendicular to the substrate holder. A special holder was constructed to preform these measurements. For these measurements an integration time of twenty seconds was used.

CHAPTER VII: ELECTRICAL CHARACTERIZATION

To complement the optical characterization of the samples produced for this project, electrical characterization by four-point probe method was done. This chapter will discuss this method and some of its results.

Background

One of the most important electrical parameters of semiconductors is the resistivity. Resistivity is important for devices because it contributes to the device series resistance and leads to ohmic heating of the devices. This parameter is an intrinsic electrical property that depends on the free electron and hole densities n and p, and the charge carrier's mobilities. The resistivity, defined as ρ is given by:

$$\rho = \frac{1}{q(n\mu_n + p\mu_p)} \tag{7.1}$$

where μ_n and μ_p are the charge carrier's mobilities, q is the elementary charge, and the resistivity is measured in Ωcm.

For thin films, the sheet resistance, ρ_s, is often used instead of the resistivity. This sheet resistance is defined as the resistivity divided by the films thickness, t. Resistivity (or its inverse, the conductivity σ in $\Omega^{-1}\text{cm}^{-1}$) and its variation with temperature is often used to classify materials into metals, semiconductors and insulators.

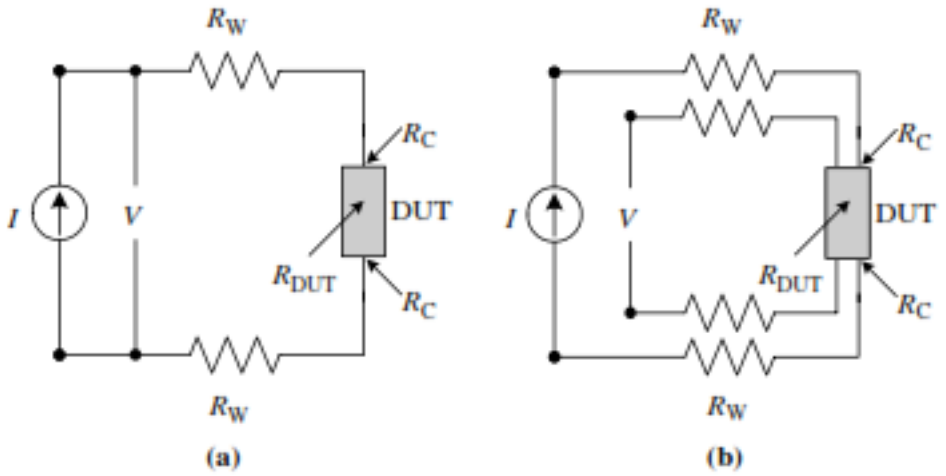

Figure 7.1: Two-Point(a.) vs. Four-Point(b.) Resistance Arrangements

Four-Point Probe Background

The simplest way to determine resistivity is to measure the voltage drop along a uniform semiconductor bar through which a DC current, I, flows. The measured resistance and the geometrical dimension can be used to estimate the resistivity. The most commonly used technique to determine the resistivity is the Four-Point Probe measurement method.

The four-point probe measurement is an absolute measurement without resorting to calibrated standards and is sometimes used to provide standards for other resistivity measurements. Two-point probe methods would appear to be easier to implement, because only two probes need to be manipulated. But the interpretation of the measured data is more difficult. Consider the two-point probe or two-contact arrangement of Figure7.1(a). Each electrode carries a current and serves as a voltage probe. The resistance of the device under test (DUT) is the parameter of interest.[27] The total measured resistance R_T contains three

contributions:

$$R_T = \frac{V}{I} = 2R_W + 2R_C + R_{DUT} \tag{7.2}$$

where R_W is the wire or probe resistance and R_C is the contact resistance and R_{DUT} is the resistance of the device under test. The measured resistance includes the contact resistance(R_C). The contact resistance can be significant for small electrodes and is strongly dependent on the electronic structure of the sample electrode interface. Equation 7.2 also includes the probe resistance, which is a complicated value that takes into account the radius of the tip of the probe that makes contact with the sample. So the interpretation of electronic transport measurements taken by a two-point probe can be difficult.

These factors are overcome by adding two more probes making a four-point probe measurement. For this method, two probes are used for current injection and the other two probes are used to measure the electric potential difference between two points of the sample. The more usual probe geometrical configuration is when the four probes are placed in a line, as shown in Figure 7.2.

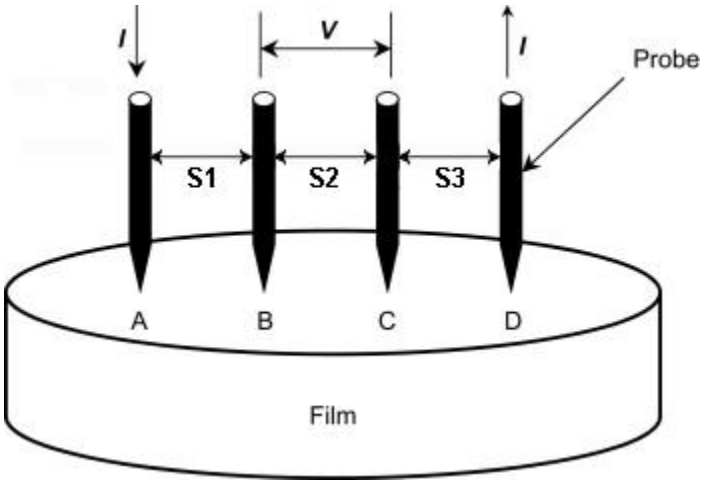

Figure 7.2: Linear Four-Point Probe Configuration

The electric potential at probe 2,induced by the current flowing from probe 1

to probe 4 is given by:

$$V_2 = \frac{\rho I}{2\pi}\left(\frac{1}{s_1} - \frac{1}{s_2 + s_3}\right) \tag{7.3}$$

where ρ is the resistivity, I is the injected current, and S_1, S_2, S_3 are the electrode spacing. At probe 3 the potential is given by:

$$V_3 = \frac{\rho I}{2\pi}\left(\frac{1}{s_1 + s_2} - \frac{1}{s_3}\right) \tag{7.4}$$

Now to find the voltage drop across the two probes we take $V = (V_2 - V_3)$ providing us with:

$$V = \frac{\rho I}{2\pi}\left(\frac{1}{s_1} - \frac{1}{s_2 + s_3} - \frac{1}{s_1 + s_2} + \frac{1}{s_3}\right) \tag{7.5}$$

After measuring this voltage and knowing the current supplied to the four-point system, the resistivity can be found by rearranging the above equation and arriving at:

$$\rho = \frac{2\pi}{1/s_1 - 1/(s_1 + s_2) - 1/(s_2 + s_3) + 1/s_3}\frac{V}{I} \tag{7.6}$$

To simplify this equation even further, most four-point probes have evenly spaced spacings. This means that $s = s_1 = s_2 = s_3$, given:

$$\rho = 2\pi s\frac{V}{I} \tag{7.7}$$

Equation 7.7 is valid only for semi-infinite samples, that is, both the sample thickness and the sample surface are very large (approaching ∞), and the probes locations must be far from any boundary. Because these relations can be applied only too large ingots, in many cases, a correction factor F must be introduced in order to take into account the finite thickness and surface of the sample and its boundary effects. Thus, the previous equation becomes:[31]

$$\rho = 2\pi s\frac{V}{I}F \tag{7.8}$$

For thin films were $t < s/2$, which covers most of the practical cases, because the probe spacing is usually on the order of a millimeter; this correction factor is related to the thickness and is given by:

$$F = \frac{(t/s)}{2ln2} \tag{7.9}$$

Providing a resistivity equation, governed by the sample thickness, to be:

$$\rho = 4.532t\frac{V}{I} \tag{7.10}$$

If the probe header is too close to any boundary, then the above equation is no longer valid and another correction factor must be introduced. This correction factor is close to 1 as long as the ratio a/s is greater than 2, where a is the distance from the edge of the sample to the first electrode.[31] It can be see from equation 7.8 and 7.10 that the four-point measurement results only measure the sample properties. Since the voltage electrodes no longer carry a significant current, no electric potential is measured across their contacts. So wire resistance and contact resistance no longer shows up in the measurement data.

Experimental Setup

A linear four point probe setup based on a 7065 Keithley Hall effect card, a 7001 Keithley switching unit, and a Jandel Linear four point probe was used to characterize low and high resistive samples. The setup includes a 2182 nanovoltmeter, a 6514 electrometer that is used to measure the current, and a 6221 current source. Guarded triax cables are used between the Hall card and the four point probe fixture, as well as between the current source and the Hall card, and between the amp meter and the Hall card. The connections within the Jandel fixture are all coaxial cables whose grounds are connected to the metal Faraday cage

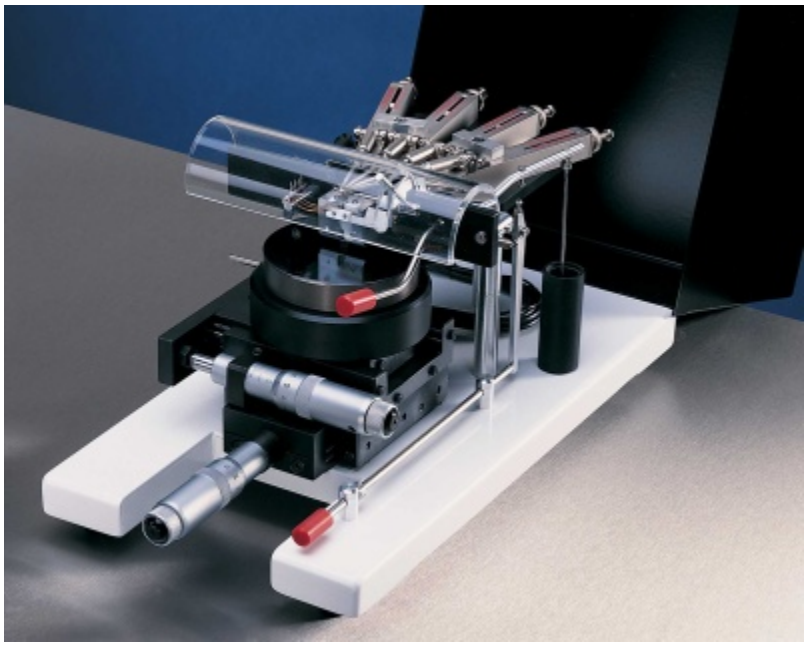

Figure 7.3: The Jandel Linear Four-Point Probe

surrounding the fixture. This fixture can be seen in Figure 7.3 and a circuit diagram of the four-point probe in Figure 7.4.

Operation of the four-point probe is straight forward. After placing the sample on the puck, the tungsten carbide probes are lowered onto the sample. The user has complete control of the speed(approximately 1 mm/sec) with which the electrodes are lowered on the sample surface and the pressure that each electrode exerts on the sample(0-100 grams). This is so that the user can control any possible damage to the sample. The probe guidance system is kinematic and free of lateral play and positions the electrodes on the sample with an accuracy of 10 μm. The needles are positioned by upper and lower jeweled guides consisting of spring-loaded ruby balls. With the probes down, the measurement can be taken. The measurements are taken using a program built in LabView. This interface is very simple to use and allows the user to vary the current that is passed through the sample. There are two different measurements modes, a low resistive mode and a high resistive mode. For low resistive samples the nanovoltmeter is directly

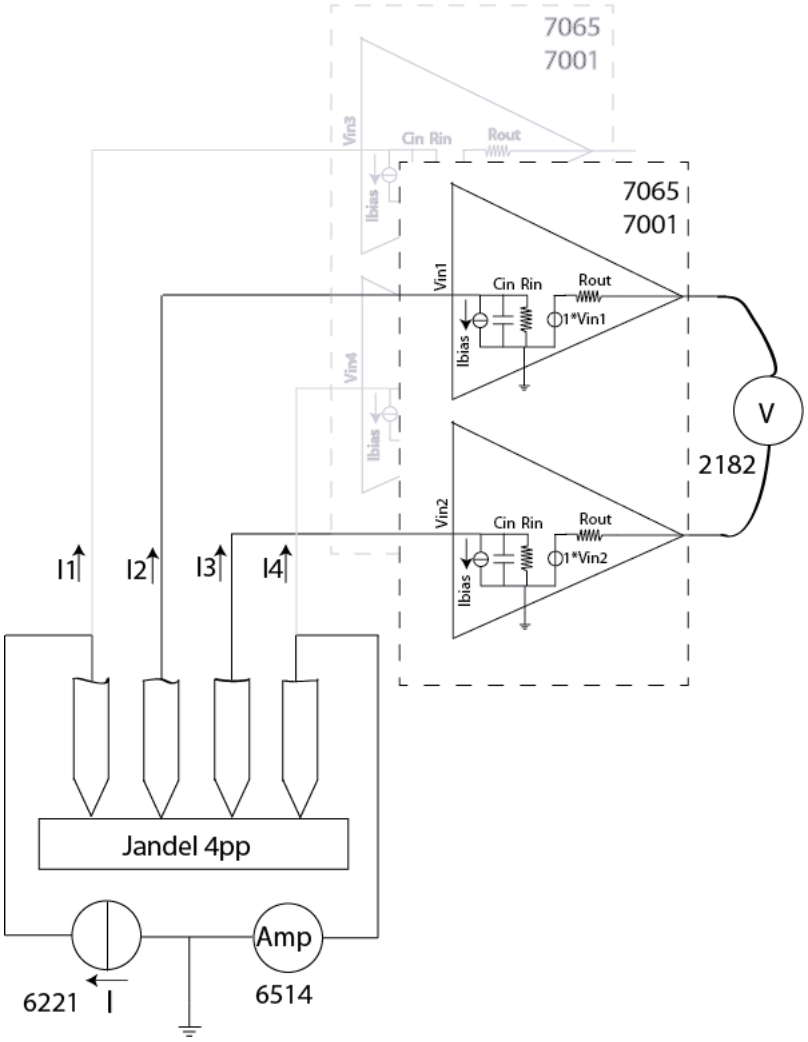

Figure 7.4: The Circuit Diagram for the Four-Point Probe

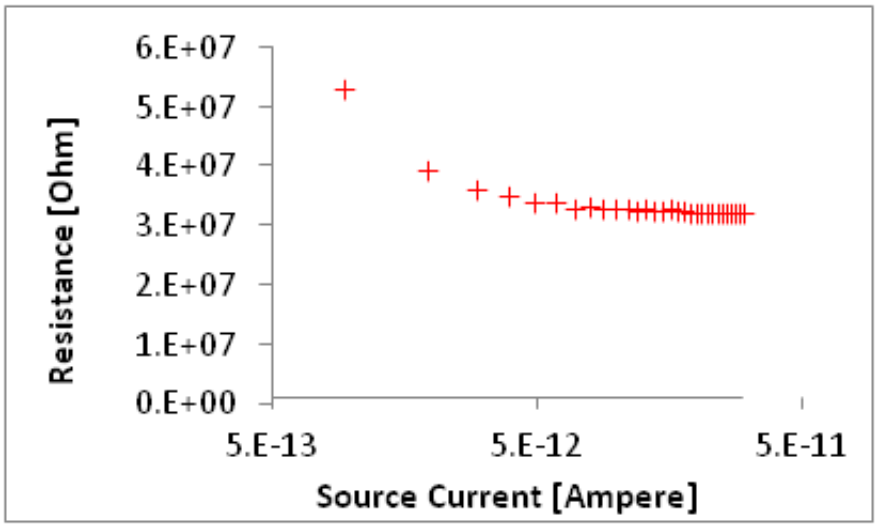

Figure 7.5: Resistance of Highly Resistive ITO Sample

connected to the sample which results in a low noise measurement with the rms noise down to several nanovolts.

For high resistive samples the 7065 Hall card needs to be used in high resistive mode. In this mode buffer amplifiers with a large input resistance (100 TΩ), a small input capacitance (3 pF) and a low input bias current (<150 fA) are switched between the sample and the voltmeter. These buffer amplifiers have an amplification of 1x and will reduce the current that flows through the voltage electrodes of the four point probe, reducing the error voltages across the voltage electrode to material contacts. When measuring high resistive samples at very small currents, the measured resistance of the setup becomes a function of the source current. Figure 7.5 shows the measured resistance of a highly resistive indium tin oxide sample as a function of the source current. A positive current was sourced through the two outer electrodes or through the two inner electrodes of the four point probe. The voltage was measured across the other two electrodes. The current source ammeter circuit and the voltmeter was switched in all 8 possible configurations using the switching capabilities of the 7001 unit. One can see that for low source currents, the measured resistance goes up by a factor of almost 10. The

data points measured at 1x10^{-14}A is realized by fine tuning the current source so the measured current is minimum but still positive.

It is believed that the measured higher resistance values for this particular sample are not due to a higher sample resistance values at low currents, but are a measurement artifact and are caused by the input bias current of the buffer amplifiers on the 7065 card. As mentioned above these buffer amplifiers are not ideal as they draw a small bias current, their input resistance is not infinity, and their input capacitance will charge or discharge upon changing the electric potential of the electrodes. So each error current consists of a time dependent exponential increasing or decreasing component originating from the charging/discharging of the input capacitor, a component proportional to the electrode potential, and a constant offset component originating from the input bias current of the buffer amplifiers:

$$I_n = I_{C_{in,n}} + I_{R_{in,n}} + I_{bias,n} = C_{in,n}\frac{dV_n}{dt} + \frac{V_n}{R_{in,n}} + I_{bias,n} \tag{7.11}$$

The first contribution is negligible if one waits long enough for the input capacitors in the buffer amplifiers to charge or discharge after a change of the source current. The 2nd contribution can introduce measurement errors on high resistive samples in two ways: (a) The input resistance shunts the sample resulting in a measured resistance that is lower than the sample resistance; (b) The voltage electrodes will draw a small current which causes an electric potential across the voltage electrodes. This can lead to an error voltage in the measured electric potential across the voltage electrodes. This error voltage can be significant for samples that make high resistive contacts to the tungsten carbide electrodes. Note that in general the voltage electrodes are at a different electric potential resulting in different electrode currents. Also the last current contribution in equation 7.11 can cause errors in the measured resistance values: (a) as part of the current leaks out of each electrode,

the charge transport between each two electrodes differs and is different from the total current sourced through the setup; (b) as the bias current is slightly different for each buffer amplifier, errors are introduced in the measured voltage for samples that make high resistive contacts to the tungsten carbide electrodes.

For this particular ITO sample, the last contribution of equation 7.11 is the dominant factor. Tungsten carbide (work function 4.9 eV) makes an Ohmic contact with ITO (work function 4 to 5 eV), and the total contact potential across any of the contacts is not larger than a couple of millivolt. So the current through the input resistors of the buffer amplifier is less than $1\text{x}10^{-18}$ amp which is significantly less than the typical input bias current of the buffer amplifiers, i.e. 150 femtoamps, and the typical offset input bias current variations of instrumentation amplifiers, i.e. $1/3 * I_{bias}$=50 femtoampere.

As the electrode to ITO contacts have a negligible Ohmic contact resistance the sample fixture system is a linear system and one can use superposition to correct for the buffer amplifier input currents. In a linear circuit the voltages and currents are a linear combination of the current and voltage sources. Thus:

$$\Delta V = V_+ - V_- = \alpha I_{sample} + \sum_{n=1}^{4} \beta_n I_{bias,n} \tag{7.12}$$

Where $\alpha, \beta_1, \beta_2, \beta_3, and \beta_4$ are constants independent of the current. Furthermore, assume that $I_{bias,n}$ are the input currents of the buffer amplifiers and are independent of the time. So if one measures ΔV at two different sample current values one can subtract out the effect of the input bias currents using the following equation:

$$R = \frac{\Delta V_2 - \Delta V_1}{I_2 - I_1} \tag{7.13}$$

The IV relation of this highly resistive ITO sample was measured as a function of

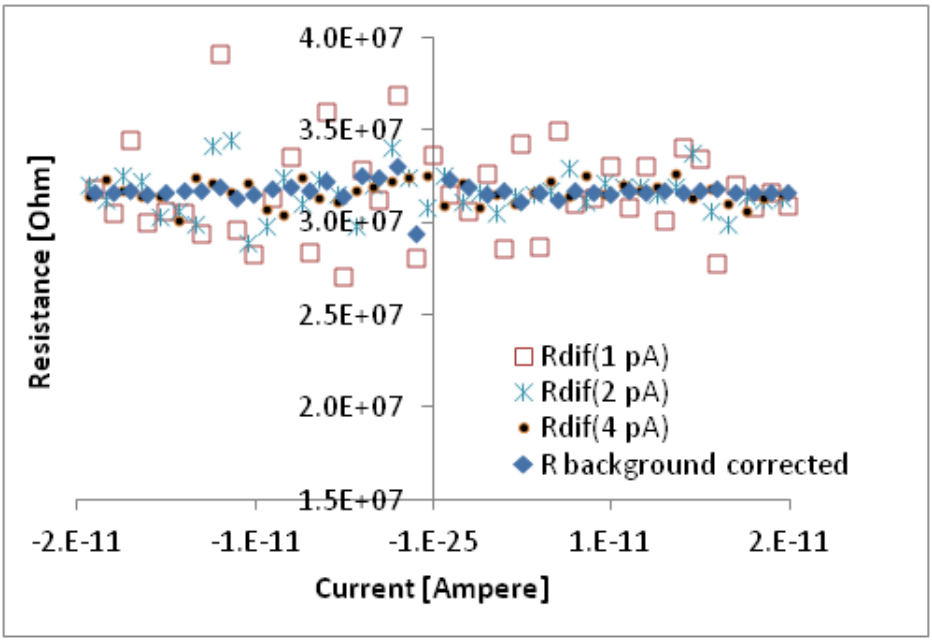

Figure 7.6: Multiple Current Measurement of ITO Sample

the source current and the resistance was calculated from two consecutive IV measurements and the resistance using equation 7.13. The quality of the offset correction depends on the sample resistance as well on the $I_2 - I_1$ term. Figure 7.6 shows the calculated resistance for three different $I_2 - I_1$ values, i.e. 1, 2, and 4 pA. Notice that the source current is not very well defined as each data point is determined by two different current measurements. Also the calculated values become rather noisy if the two corresponding data points are close in value(compare R_{1pA} with R_{4pA}). The farther the two currents were apart the smaller the data points were scattered. A less noisy correction can be made by using all the data points to determine the offset current. This can be done by doing a least square fit on all IV-data points and calculate the offset current. Then this offset current can be used to correct all measured currents before the resistance is calculated. The result of such correction introduces less noise, and each resistance value is mainly determined by the I-V values measured at that particular current value (see diamonds in Figure 7.6).

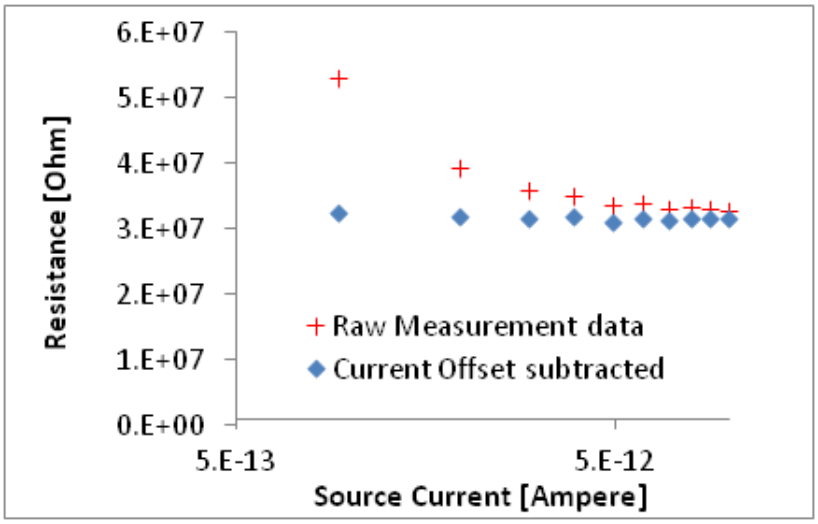

Figure 7.7: The Measured Resistance of High Resistive ITO Sample with and without Offset Correction

Figure 7.7 shows the measured resistance values as a function of the source current using no corrections (red crosses) and using the offset correction (blue diamonds) for this high resistive ITO sample. The correction improves the accuracy of the setup and extends the measurement range with a little over one order of magnitude.

After the correction was factored into the four-point probe setup, a test to see if the samples are homogeneous was preformed. The test consisted of measuring the resistance at regular intervals across the width and length of the sample. Sample 032713A was chosen for this test. The results can be seen in Figures 7.8 and 7.9. From these values, the standard deviation was calculated and divided by the average measurement value and found +/- 1.5% for across the width of the slide, and +/-3% across the length of the slide, which shows that the ITO film is homogeneous across the entire slide.

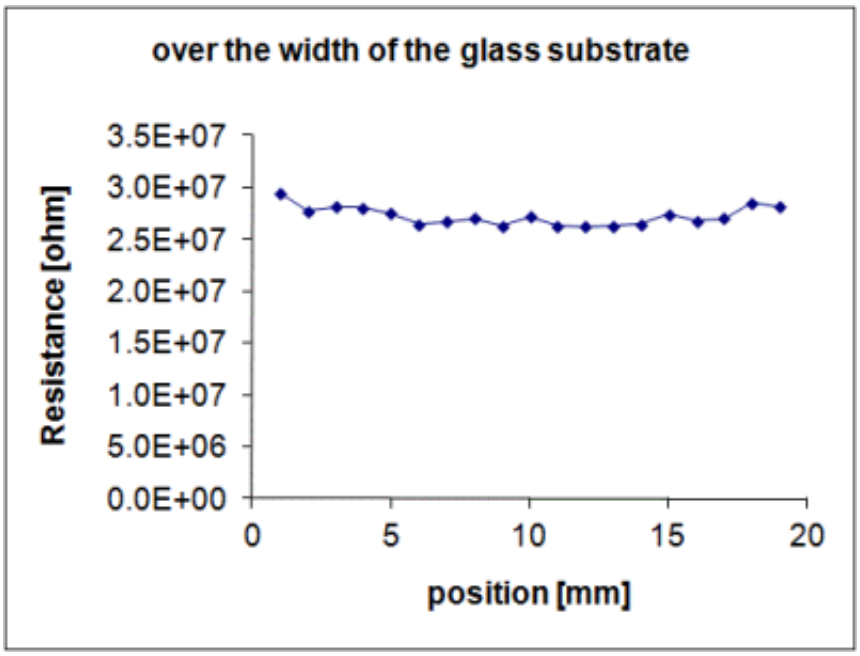

Figure 7.8: Resistance Distribution Across the Width of the Slide

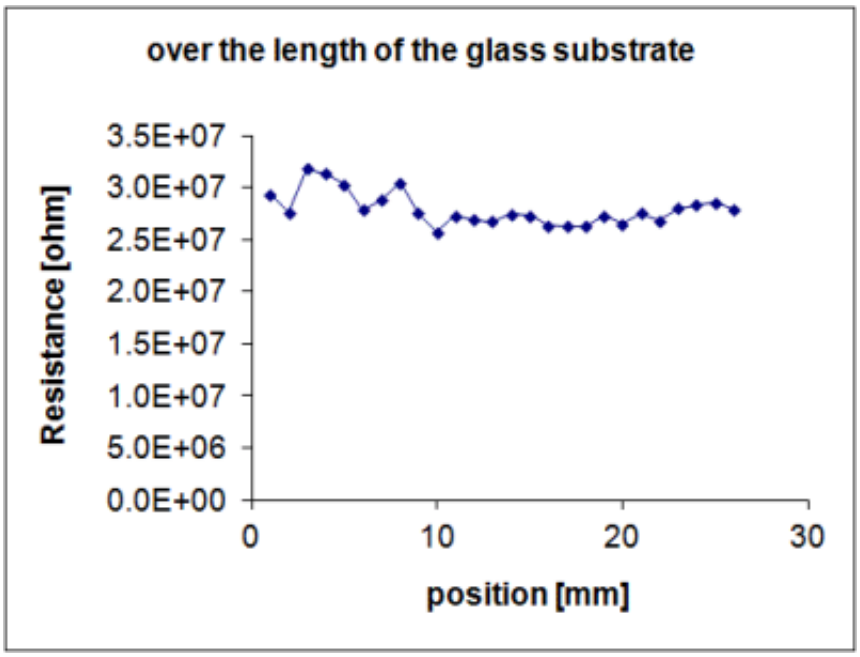

Figure 7.9: Resistance Distribution Across the Length of the Slide

CHAPTER VIII: RESULTS

This chapter will present the results of the measurements performed on the samples that were deposited by DIBS. The data will be presented in two sections: one for the ellipsometric data and one for the electrical characterization.

Ellipsometric Data

The data that were obtained through the procedures outlined in Chapter 6, was used to determine the film thickness of the SiO_2 buffer and ITO layers as well as the optical properties of the substrates, the SiO_2 buffer layer, and the ITO film.

The optical properties of the glass substrate is the first to be investigated. The transmission spectra of the glass microscope slides is given in Figure 8.1. The transmission is approximately 0.9 from 1000 to 315 nm and then decreases strongly to zero below 280 nm. The 90% transmission is not caused by absorption in the glass but by the reflected light. Light is reflected off the sample because its index of refraction is different from air. At perpendicular incidence the influence of the reflection on the transmission coefficient of a transparent sample is given by:

$$T = \frac{2n}{n^2 + 1} \tag{8.1}$$

The transmission spectra suggest that the index of refraction of the microscope slide is approximately 1.5. Below 315 nm the glass starts to show significant absorption as shown by the transmission spectra. The optical properties of the glass microscope slides were determined from the measured ellipsometry and transmission

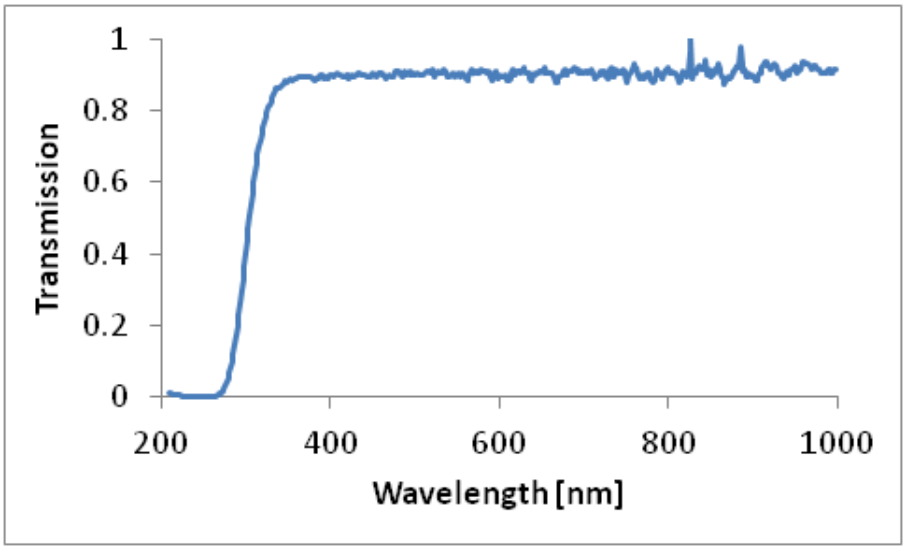

Figure 8.1: Transmission of Light through Glass Slide

spectra. A spline model was used along with the ellipeometric data, that has been appended with the transmission data (B-spline resolution = 0.3 eV, starting materials = Glass slide.mat). When a roughness layer was fit to the model it decreased the MSE from 4.7 to 3.1 and was calculated to be 12.1 Å. The calculated spectra are shown in Figure 8.2:

The thickness of the SiO_2 buffer layer is the next point of interest. The model that was used started with a bulk silicon model(Si_JAW), with a native oxide layer(NTVE_JAW) of 17.89 Å, and then the oxide is Modeled by SiO_2_JAW. Only silicon samples were used here because the optical constants for SiO_2 are so close to that of the glass slides because the composition of the slides contains SiO_2. No roughness was included into this fit. Also the angle offset was fixed at 0 degrees. The ellipsometric data from 400 nm and up were used for fitting this model. The following results were obtained:

1. 031613A: 7 sccm molecular oxygen, 20 minutes sputter time: d=1364 A (51 MSE): sputter rate = 6.8 mm/min

2. 032013P: 4 sccm atomic oxygen, 20 minutes sputter time: d=1463 A (58

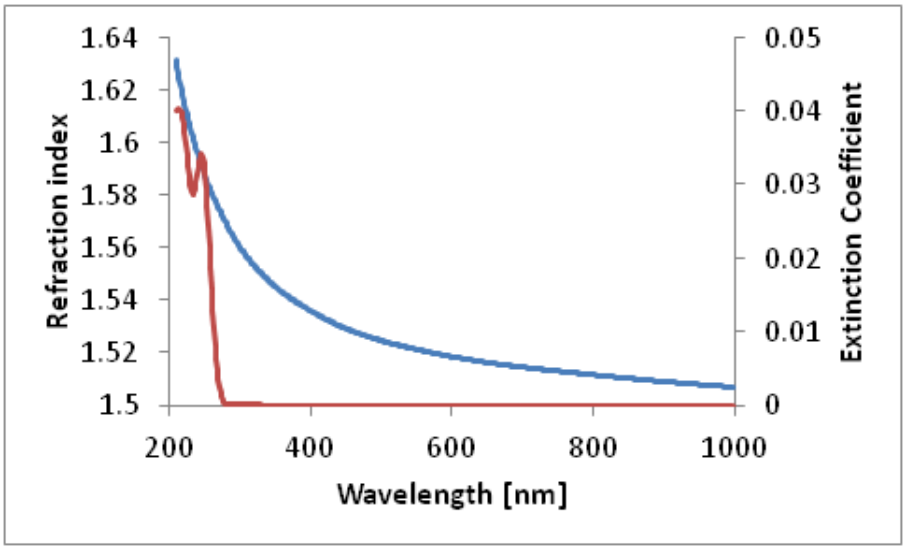

Figure 8.2: Optical Properties of the Glass Slides; Refraction in blue and Extinction in blue

MSE): sputter rate = 7.3 mm/min

3. 032813A: 4 sccm atomic oxygen, 4 minute sputter time: d=288A (6.9 MSE): sputter rate = 7.2 mm/min

The results show that the sputter rate for atomic oxygen at 4 sccm is larger than the sputter rate for molecular oxygen at 7sccm. The thickness ratio of the thick and thin SiO_2 film deposited with 4sccm atomic oxygen is 5.08 which is expected as their deposition time also varies with a factor 5. Note the much lower MSE for the thinner film. For thinner films the ellipsometric quantities are less sensitive to the optical properties relative to the thicker film. The sputtered SiO_2 was modeled by SiO_2_JAW which are the optical properties of thermally grown SiO_2. The larger MSE for the thicker films suggest that the sputtered SiO_2 might have slightly different optical properties from the used SiO_2_JAW data in the model. An attempt was made to determine the optical properties of the SiO_2 using the measurement data on the silicon substrates but was abandoned as the calculated spectra were too strongly coupled to the optical properties of the silicon substrate showing the short

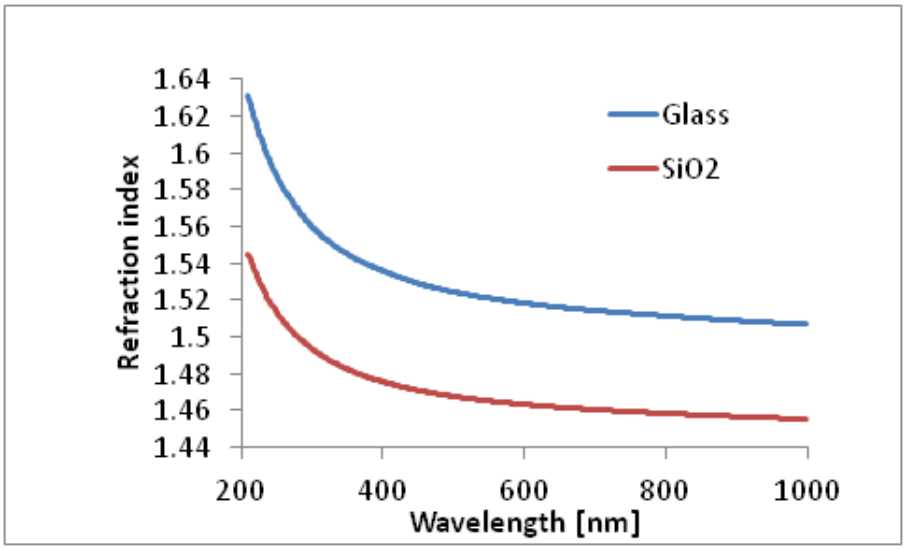

Figure 8.3: Index of Refraction of SiO_2

wavelength silicon peaks.

The samples sputtered on silicon looked more homogeneous than the SiO_2 samples sputtered on Glass to the naked eye. The light that reflected off of them had a purple glow on one side and was white on the other side. The purple glow indicates that the thin film acts as an anti-reflection coating as both the blue and red parts of the incident light are preferentially reflected. In transmission the SiO_2 had slightly more absorption on the purple-side. It is not clear why the film on the glass substrate is inhomogeneous as the substrate is rotated during deposition.

Next, the spectroscopic data of the ITO samples on glass were used to determine the film thickness. The following model was used: the glass B-spline model described above with ITO(GenOsc) on top. Again, roughness was not included as a fit parameter and only the ellipsometric data appended with the transmission data from 700 to 1000nm was used. It was noticed that the samples sputtered at higher oxygen flow rates had a lower MSE. From this it can be concluded that the optical properties of the samples sputtered at lower oxygen flow rates differed significantly. This is in agreement with the transmission data where

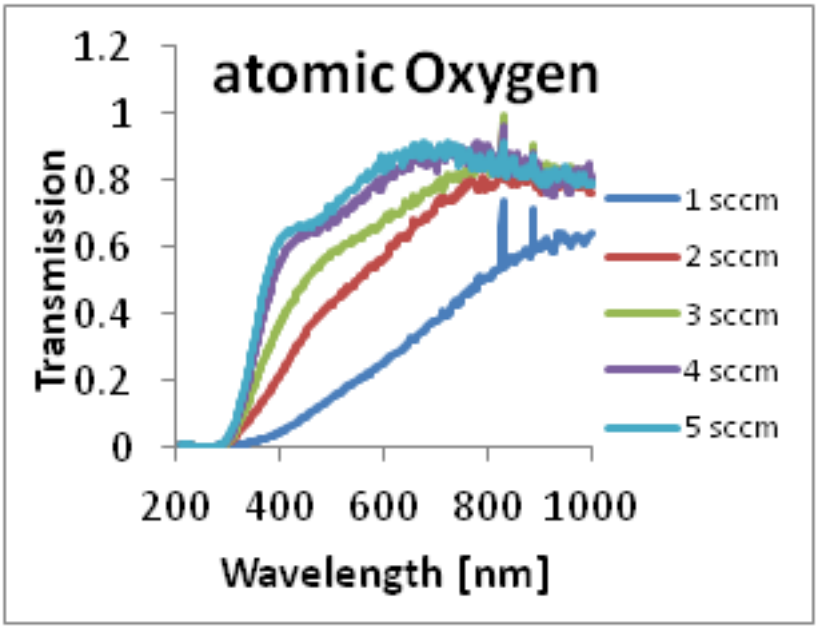

Figure 8.4: Transmission vs. Wavelength for Atomic Oxygen Samples

the transparency increases for higher oxygen flow rates. Comparing Figures 8.4 and 8.5 no large differences in the shape of the spectra was observed. The average value for the thickness of the ITO film was approximately 185nm. This corresponds to a deposition rate of 2.3 Å/sec. The deposition rate was approximately independent of the oxygen flow rate.

Finally the optical properties of the ITO films were examined. To determine the optical properties from the ellipsometeric data, it is not possible to do a point by point fit of the n and k values as also the thickness of the ITO needs to be determined from the data. Therefore the following experimental facts were used to make a model for the DIBS sputtered ITO samples:

1. ITO is a degenerate n-type semiconductor with a bandgap of 3.75 eV meaning that ITO contains a lot of free electrons. It is furthermore expected that its remains transparent for photon energies below the bandgap.

2. Previous experiments at Texas State University[20] have shown that the ITO

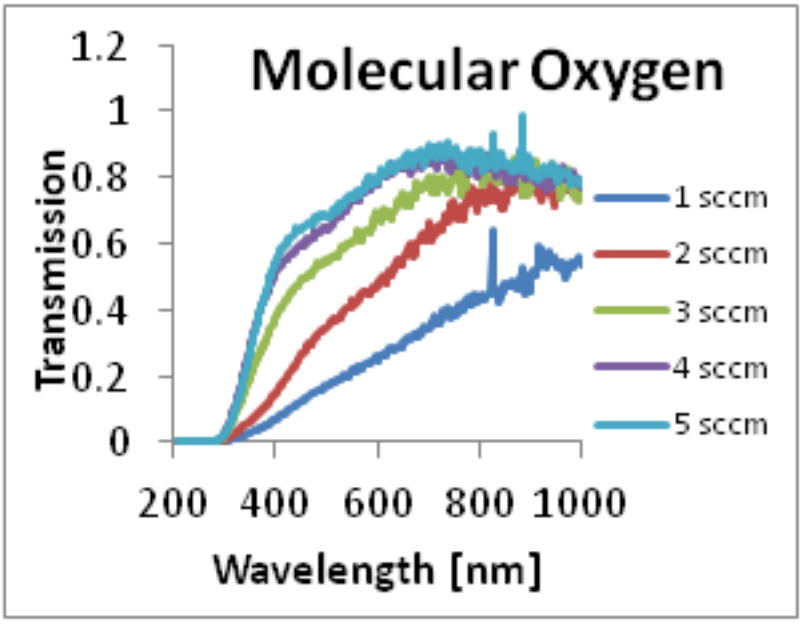

Figure 8.5: Transmission vs. Wavelength for Molecular Oxygen Samples

films grown by DIBS at room temperature are amorphous. Figure 8.6 shows the X-ray spectra of DIBS ITO films grown at four different temperatures. The sample grown at room temperature shows a smooth curve and sharp diffraction peaks are missing in the two theta scan. This indicates that the crystallites for the room temperature samples are too small and in general one assumes such material to be amorphous.

3. AFM scans on ITO samples previously sputtered at Texas State show that typical rms roughness values are in the 1- 3 nm range and vary with the substrate temperature and oxygen pressure. No noticeable difference was observed when comparing ITO films deposited on Silicon or on glass. Figure 8.7 shows an AFM image of the 2sccm atomic oxygen sample sputtered on glass. It has an rms roughness of 1nm.

To get an idea of the optical properties the ellipsometry data of the samples on Silicon were used to determine the n and k of the ITO. The model is as follows: bulk silicon(Si_JAW), with a native SiO2(NTV_JAW)layer, then included a

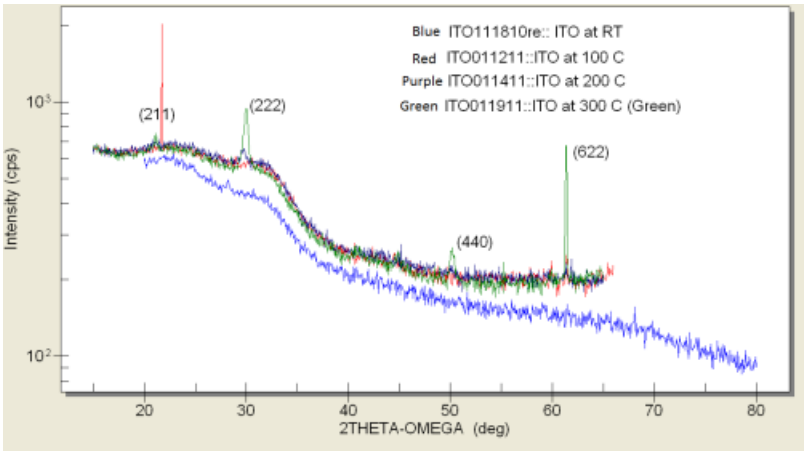

Figure 8.6: Two Theta Scan of ITO sputtered by DIBS. Angle of incidence of oxygen beam is 85°[20]

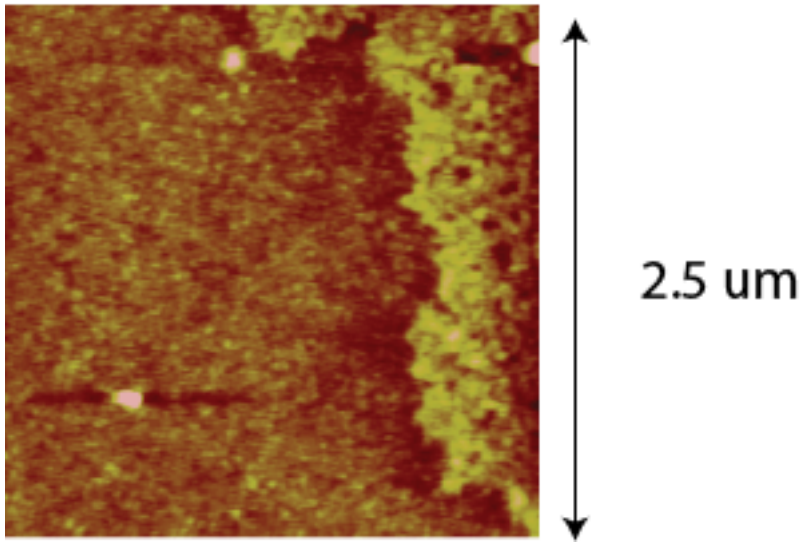

Figure 8.7: AFM Image of ITO on Glass Sputtered at 2sccm Atomic Oxygen

SiO_2(SiO_2_JAW) buffer layer of 28.8 nm thickness, then finally an ITO(ITO(GenOsc)) layer. A good model for ITO was found in the Woollam database. It consisted of three different optical contributions, i.e. a Tauc-Lorentz contribution, a Gaussian contribution, and a Drude contribution. The motivation for this model was as follows:

1. A 20 Å roughness was included in the model because of the previous AFM measurements on the ITO samples mentioned above.[20]

2. As mentioned above the DIBS ITO samples sputtered at room temperature are amorphous. The absorption band of amorphous and glassy films often has a Gaussian shape. The atomic bonds lengths and angles are randomly distributed around average values. As each absorption band consists of numerous harmonic oscillators whose resonant frequencies have a normal distribution the absorption peaks in amorphous materials has a Gaussian character.[32]

3. ITO is a degenerate semiconductor. Tauc Lorentz models are normally used to model amorphous semiconductors above and below the bandgap.[33]

4. The Drude contribution to the optical properties is caused by the free electrons in the ITO.[34]

The typical relative magnitude of each contribution is shown in Figure 8.8 It can be seen from the graph that an increasing extinction coefficient for larger wavelengths is an indicator for a contribution of the free electrons to the optical properties. This is important as an increase of the absorption toward the longer wavelengths corresponds to a less resistive film. No attempt was made to determine the resistivity from the Drude contribution.

For most samples all parameters were fit which includes: (1) the thickness;

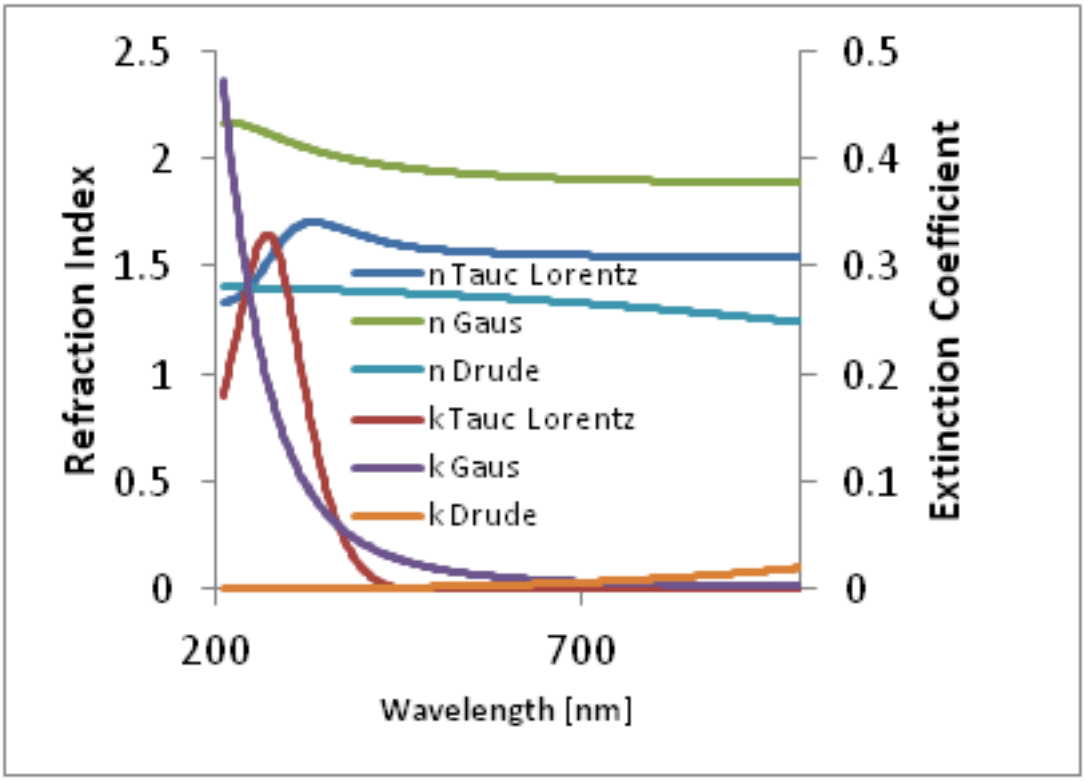

Figure 8.8: Optical Properties of ITO Due to the Fit Models

(2) four parameters describing the Tauc-Lorentz model; (3) 3 parameters describing the Gaussian contribution; (4) 2 parameters describing the Drude contribution. For samples sputtered at 1 sccm and 2sccm the resistivity was fixed at the value measured by four-point probe, otherwise the Drude parameters would become non-physical. Graphs of the refraction and extinction coefficient for all ITO samples sputtered on silicon are given in Figures 8.9 and 8.10.

The extinction coefficient graph was converted in an absorption coefficient using equation 6.5 and are shown in Figures 8.11 and 8.12 The absorption of the ITO films appears to decrease with larger oxygen flow rate. A Drude contribution to the optical properties was observed for the samples sputtered at 4 and 5 sccm. The atomic oxygen samples are a little more transparent then the samples deposited with molecular oxygen.

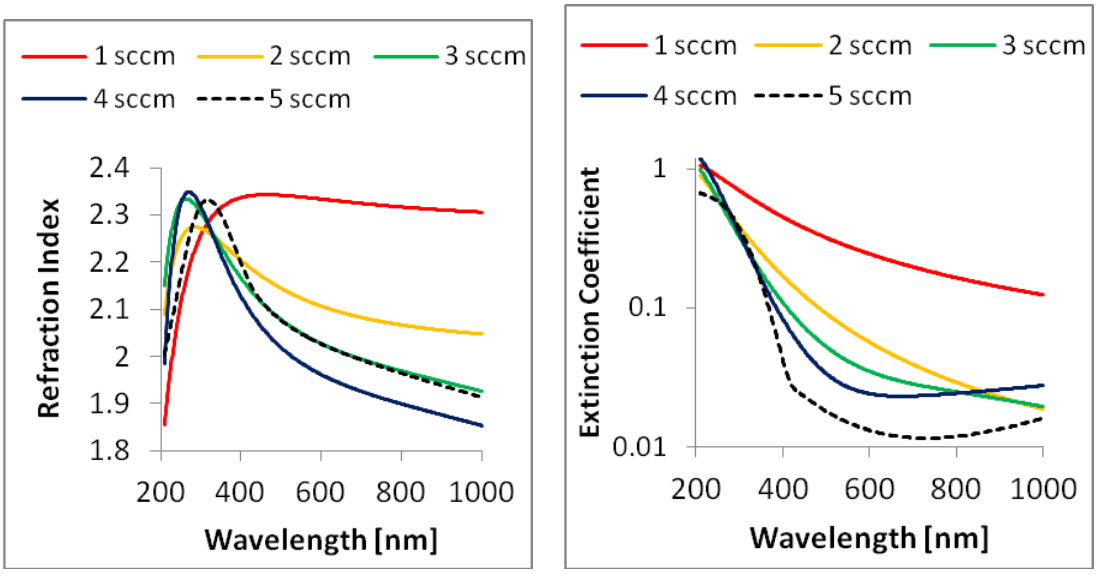

Figure 8.9: Optical Properties for ITO Sputtered with Atomic Oxygen

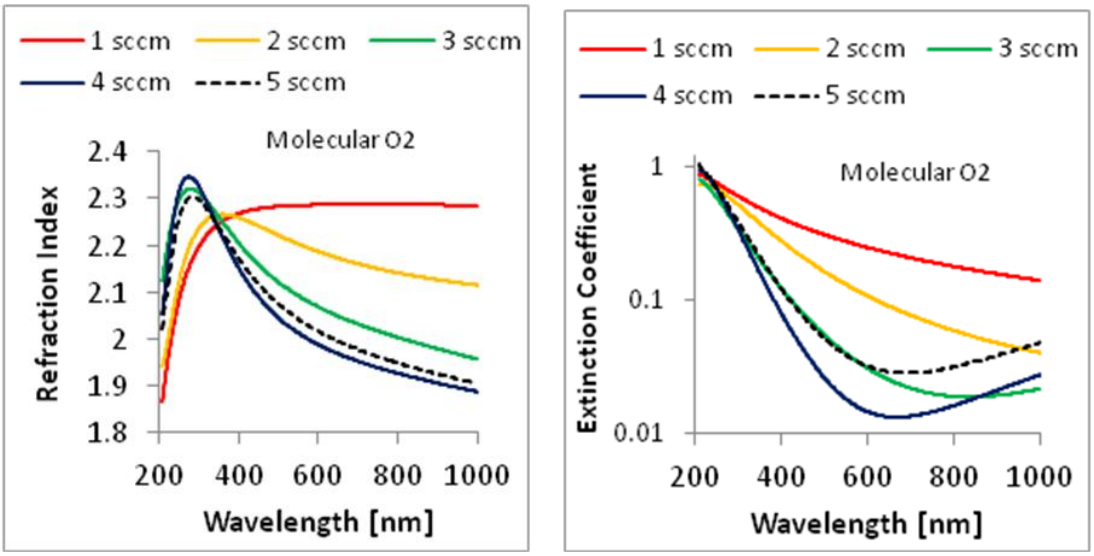

Figure 8.10: Optical Properties for ITO Sputtered with Molecular Oxygen

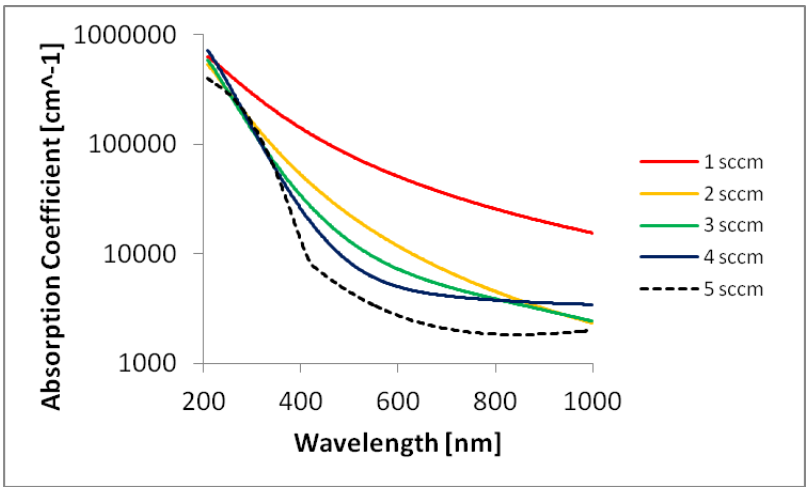

Figure 8.11: Absorption Coefficients of ITO Sputtered with Atomic Oxygen

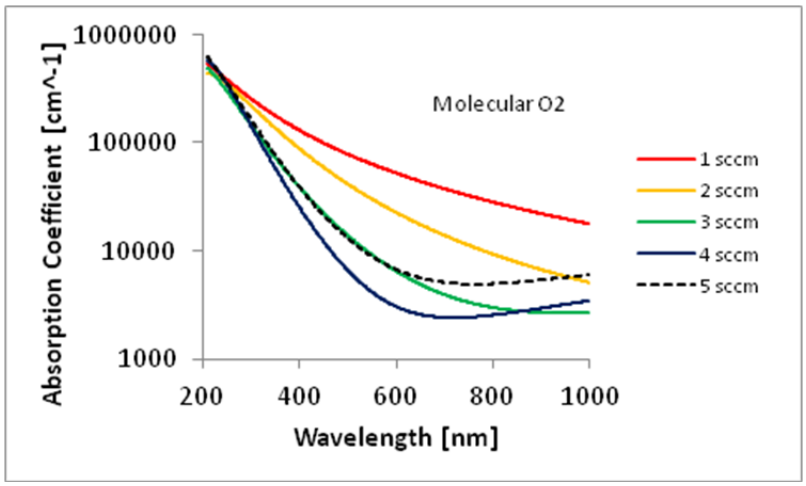

Figure 8.12: Absorption Coefficients of ITO Sputtered with Molecular Oxygen

Electrical Properties

The four-point probe sheet resistance of the samples was measured with the setup described in the previous chapter. The electrode pressure of the Jandel probe was set to 85 grams and the descent rate of the electrodes to 1 mm/sec. Measurements were done for a current close to the maximum source current(samples sputtered at 1sccm) or 1 μA(samples sputtered at 2-5 sccm).

1. ITO samples on silicon: The ITO samples on silicon all had a very low sheet resistance close to the sheet resistance of the substrate. This suggests that the oxide layer is not continuous or that the electrodes of the four point probe pinch through it.

2. ITO samples on glass: The resistance of the ITO samples on glass are shown in Figure 8.13. For Oxygen flows equal or larger than 2 sccm, the samples sputtered by atomic oxygen had a lower resistance than the samples sputtered using molecular oxygen. The samples that were sputtered at 1 sccm oxygen flow rate had a metallic luster which indicates that the film is not fully oxidized. These samples also have low conductivity and a low slope in the long wavelength side of the absorption spectra.

The calculated thickness was used to calculate the resistivity from the sheet resistance. The results are shown in Figure 8.14. The samples sputtered by atomic oxygen have a lower resistivity than the samples sputtered using atomic oxygen.

The calculated absorption spectra were used to calculate the average absorption coefficients in the visible range from 400 to 800 nm. As mentioned in chapter 1, the reciprocal value of the product of the resistivity and the optical absorption is the key figure of merit for a TCO. The calculated figure of merit can be seen in Figure 8.15. For oxygen flows larger than 2 sccm this factor is 1.2 to 3

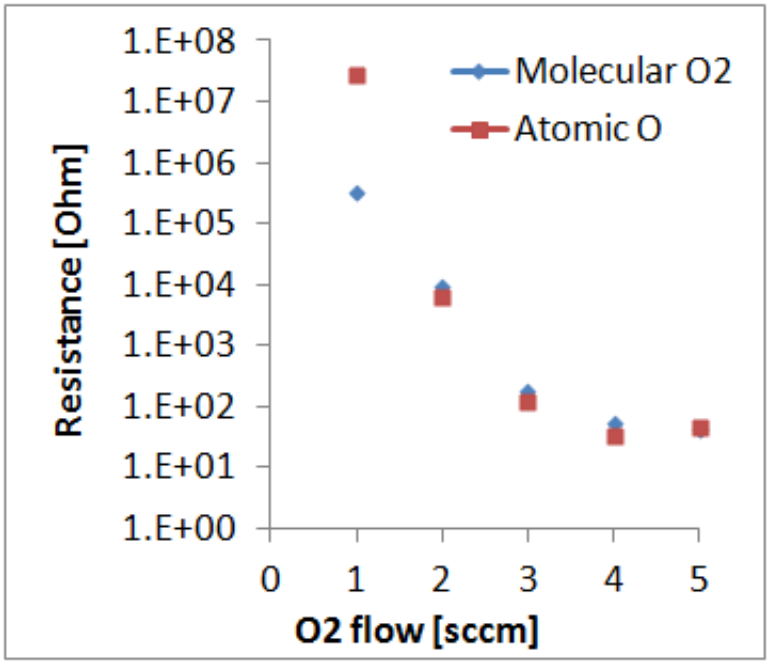

Figure 8.13: Resistance vs. Oxygen Flow Rate

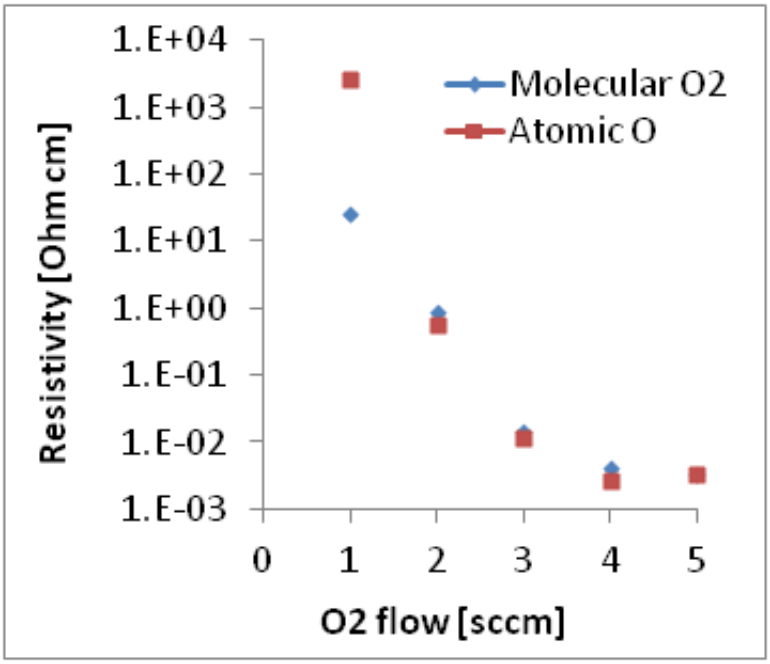

Figure 8.14: Resistivity vs. Oxygen Flow Rate for ITO

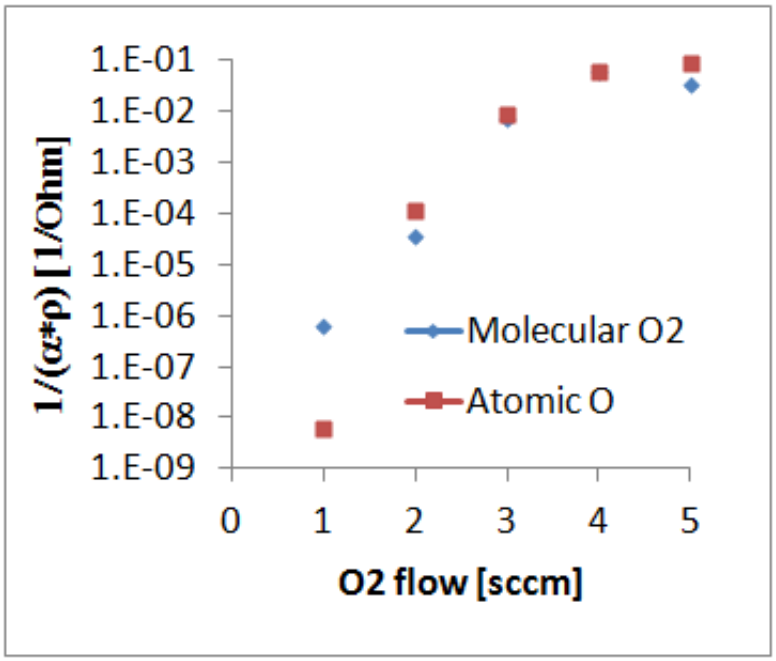

Figure 8.15: Figure of Merit for ITO Samples

times higher for ITO sputtered by atomic oxygen. The trend of the group suggests that the optimum deposition conditions for atomic oxygen might be beyond the 5 sccm oxygen flow rate.

CHAPTER IX: CONCLUSIONS

By repairing multiple vacuum system leaks and mending broken parts, the base pressure of the DIBS system was lowered from $3x10^{-6}$ torr to $1.3x10^{-7}$ torr. At this new base pressure, the monolayer formation time increased to 85 seconds. Therefore, the effect of the background oxygen pressure from any outgassing during the growth of the samples can be substantially excluded from the formation of the Indium Tin Oxide films.

ITO films were successfully deposited at room temperature onto glass microscope slides and silicon substrates. Two series of ITO films were made by DIBS by exposing the substrates to an oxygen beam during deposition. The effect of atomic versus molecular oxygen on the resistivity, the optical absorption, and the figure of merit was investigated.

It was noted that the sheet resistance and the resistivity decrease as a function of the oxygen flow rate. Additionally, these values decrease with the use of atomic oxygen. These findings confirm that sputtering with an assist beam consisting of atomic oxygen provides a better quality ITO film than sputtering with molecular oxygen. The lowest resistivity that was obtained was $2.67x10^{-3}$ Ωcm. This value was obtained at an atomic oxygen flow rate of 4 sccm, the flow rate that was found to produce the most efficient atomic oxygen flux in the HD25 atomic source. The measured resistivity is comparable to what has been obtained by others using DIBS for deposition at room temperature.

After calculating the average absorption coefficient from the calculated n and k spectra, the figure of merit was calculated. The ITO films that were deposited

with an atomic oxygen assist beam had a figure of merit that was between 1.2 to 3 times higher than the figure of merit calculated for the molecular oxygen samples. This once again indicated that the ITO films deposited with atomic oxygen are of higher quality then those deposited with molecular oxygen. The best figure of merit that was obtained from the samples was 0.08. Although this value is comparable to what others have found[11] for ITO films deposited by ion beam sputtering at room temperature, it is significantly less than TCO's deposited at optimized process parameters.[2] The figure of merit data available from literature is very sparse; the resistivity is a well defined parameter but the absorption coefficient is not. It is not always clear how the absorption coefficient is calculated from the measurement data (i.e. value of 550nm, or average value of an absorption wavelength graph, or average value of an absorption photon energy graph).

The optical properties of ITO as a function of the oxygen gas flow were determined from the ellipsometry data. For molecular oxygen the transparency increases as a function of the oxygen flow rate and reaches a maximum at 4 sccm. For atomic oxygen the transparency increases as a function of the oxygen flow and the 5 sccm sample showed the largest transparency. It is believed that samples deposited with higher atomic oxygen flow rates will have a higher transparency and better optical properties. For both type of samples the absorption increases at the longer wavelength side of the optical spectrum. It is believed that this increase is caused by the presence of more charge carriers for ITO samples sputtered at high oxygen flow rates, resulting in a larger Drude contribution. It is currently not clear what causes the observed differences in optical spectra between samples made with molecular or atomic oxygen.

As a result of this project, it becomes evident that the formation and quality of indium tin oxide films deposited by DIBS with an atomic oxygen assist beam at

room temperature is better than that of ITO films deposited with molecular oxygen present.

BIBLIOGRAPHY

[1] N. Simpson, W. Geerts, and A. Bandyopadhyay, "Optical properties of dual ion beam sputtered indium tin oxide films on glass and silicon," March 2012, presentation at APS spring meeting of the Texas Section of the American Physical Society in San Angelo, Tx.

[2] R. G. Gordon, "Criteria for choosing transparent conductors," *MRS Bulletin*, vol. 25, no. iss. 08, pp. 52–57, August 2000.

[3] B. G. Lewis and D. C. Paine, "Applications and processing of transparent conducting oxides," *MRS Bulletin*, vol. 25, no. iss. 08, pp. 22–27, August 2000.

[4] Y. Suzaki and T. Shikama, "Low-temperature preparation of ito films by dual ion beam sputtering," *Electronics and Communications in Japan*, vol. 82, no. 08, pp. 30–35, May 1999.

[5] Y. Suzaki, T. Shikama, S. Fukui, H. Higuchi, O. Tanaka, and T. Kajitani, "Effect of he ion beam irradiation on the ito films prepared by ibs method," *Journal of the Japan Society for Precision Engineering*, vol. 66, no. No. 10, pp. 1616–1620, October 2000.

[6] Y. Suzaki, T. Shikama, O. Tanaka, T. Kajtani, H. Higuchi, and S. Nakamura, "Effect of in-situ he ion beam irradiation on the ito films prepared by ibs method," in *Proceedings of the 9th International Conference on Production Engineering*, no. No. 03. SPE Publication Series, September 1999, pp. 601–605.

[7] Y. Suzaki, T. Shikama, O. Tanaka, H. Higuchi, and S. Nakamura, "Low-temperature preparation of ito films by dual ion beam sputtering," *Electronics and Communications in Japan, Part 2*, vol. 82, no. No. 5, pp. 30–35, May 1999.

[8] S. H. Lee, S. H. Cho, H. J. Kim, S. H. Kim, S. G. Lee, K. H. Song, and P. K. Song, "Properties of ito (indium tin oxide) film deposited by ion-beam-assisted sputter," *Molecular Crystals and Liquid Crystals*, vol. 564, no. Iss. 1, pp. 185–190, 2012.

[9] D. Kim, Y. Han, J.-S. Cho, and S.-K. Koh, "Low temperature deposition of ito thin films by ion beam sputtering," *Thin Solid Films*, vol. 377-378, pp. 81–86, December 2000.

[10] Y. Han, D. Kim, J.-S. Cho, S.-K. Koh, and Y. S. Song, "Tin-doped indium oxide (ito) film deposition by ion beam sputtering," *Solar Energy Materials and Solar Cells*, vol. 65, no. Iss. 1-4, pp. 211–218, January 2001.

[11] B. Lucas, W. Rammal, and A. Moliton, "Ito films realized at room-temperature by ion beam sputtering for high-performance flexible organic light-emitting diodes," *The European Physical Journal Applied Physics*, vol. 34, no. Iss. 3, pp. 179–187, June 2006.

[12] J.-S. Cho, K. H. Yoon, and S.-K. Koh, "Material properties of indium oxide films prepared by oxygen ion assisted deposition," *Journal of Applied Physics*, vol. 89, no. Iss. 6, pp. 3223–3228, March 2001.

[13] J. Bregman, Y. Shapira, and H. Aharoni, "Effects of oxygen partial pressure during deposition on the properties of ion-beam-sputtered indium-tin oxide thin films," *Journal of Applied Physics*, vol. 67, no. Iss. 8, pp. 3750–3753, March 1990.

[14] M. Bender, W. Seelig, C. Daube, H. Frankenberger, B. Ocker, and J. Stollenwerk, "Dependence of oxygen flow on optical and electrical properties of dc-magnetron sputtered ito films," *Thin Solid Films*, vol. 326, no. Iss. 1-2, pp. 72–77, August 1998.

[15] Varian, *Basic Vacuum Practice*, 3rd ed. Varian Associates, Inc.

[16] Z. Jiang, K. Cheng, and D. Harrison, "A concurrent engineering approach to the development of a scroll compressor," *Journal of Materials Processing Technology*, vol. 107, no. 1-3, pp. 194–200, November 2000.

[17] V. INC., "Dry scroll pumps," 2010. [Online]. Available: http://download.chem.agilent.com/videos/instruments/vacuum/2010catalog/documents/03_Scroll_Pumps.pdf

[18] A. Gregory, *The Effect of Plastic Deformation on a Series of Thin Magnetic Films*. Texas State University-San Marcos, December 2010.

[19] SiliconFarEast.com, "Residual gas analysis," 2005. [Online]. Available: http://www.siliconfareast.com/rga.htm

[20] A. Woodall, W. Geerts, and A. Bandyopadhyay, "Electrical and optical properties of ito films prepared by dual ion beam sputtering," March 2011, poster presentation at APS meeting in Dallas, TX.

[21] C. B. S. Company, "Microscope slides," 2012. [Online]. Available: http://www.carolina.com/microscope-slides-covers/microscope-slides-carolina-glass-standard-25-x-75-mm-096-106-mm-box-72/632010.pr?question=

[22] A. Gonzalez-Elipe, F. Yubero, and J. Sanz, *Low Energy Ion Assisted Film Growth*. Imperial College Press, 2003.

[23] K. Wasa and S. Hayakawa, *Handbook of Sputter Deposition Technology.* Noyes Publications, 1992.

[24] B. Wolf, *Handbook of ion sources.* CRC Press, INC, 1995.

[25] AZoM, "Ion beam deposition - applications and advantages," 2012. [Online]. Available: http://www.azom.com/article.aspx?ArticleID=5862

[26] K. Wasa, M. Kitabatake, and H. Adachi, *Thin Film Materials Technology - Sputtering of Compound Materials.* William Andrew, INC, 2004.

[27] D. K. Schroder, *Semiconductor Material and Device Characterization.* John Wiley & Sons, Inc., 2006.

[28] H. G. Tompkins, *A User's Guide to Ellipsometry.* Dover Publication, Inc, 1993.

[29] J. W. Co., "Ellipsometry tutorial," 2013. [Online]. Available: http://jawoollam.com/tutorial_1.html

[30] H. G. Tompkins and E. A. Irene, *Handbook of Ellipsometry.* William Andrew, Inc, 2005.

[31] M. Deen and F. Pascal, "Electrical characterization of semiconductor materials and devices-review," *Journal of Materials Science: Materials in Electronics*, vol. 17, no. Iss. 8, pp. 549–575, August 2006.

[32] T. Tiwald, "The gaussian oscillator." [Online]. Available: http://www.jawoollam.com/Newletters/TechNotes/gaussian_oscillator.pdf

[33] G. Jellison and F. Modine, "Parameterization of the optical function of amorphous materials in the terband region," *Applied Physics Letters*, vol. 69, pp. 371–373, 1969.

[34] N. W. Ashcroft and N. D. Mermin, *Solid state physics.* Saunders College, 1976.

VITA

Nelson A. Simpson was born in Wichita, Kansas on February 23, 1987, the son of Vida Marie Simpson and Donald Ray Simpson.After completing his work at Wink High School, Wink, Texas, in 2005, he entered Angelo State University. In May 2010, he received his degree of Bachelor of Science in Applied Physics. In August of 2010, he entered the Graduate College of Texas State University-San Marcos, seeking his Master's of Science in Physics.

Permanent e-mail address: nelson.a.simpson@gmail.com

This thesis was typed by Nelson A. Simpson.